

## Reply to Editor comments

*In the following the comments of the editor are presented (black) alongside with our replies (in blue) and changes made to the manuscript (in red).*

- 5 General statement: Dear Ivan Tadic, my comments have been well answered. I still have one more question. I noted that the reaction of NO<sub>2</sub> with OH has not been discussed. Equation (4) and (7) assume that all NO<sub>2</sub> formed by reactions R4+R5 is photolyzed and converted to ozone. However, NO<sub>2</sub> can also react with OH forming HNO<sub>3</sub>, which reduces the net ozone formation rate. How does the daily production rate of HNO<sub>3</sub> compare with the NOPR shown in Figs. 8 and 9? I think this point needs some discussion.
- 10 Dear editor, we appreciate your additional comment. You are right that the conversion of NO<sub>2</sub> to HNO<sub>3</sub> via reaction with OH will reduce the net ozone formation rate. Here we assumed that all NO<sub>2</sub> formed via reactions R4 and R5 is photolyzed and converted to ozone. This is justified by the finding that the noontime ratio  $(k_{\text{NO}_2+\text{OH}}[\text{NO}_2][\text{OH}]) / (j(\text{NO}_2)[\text{NO}_2])$  varied between 0 and 1 % (average 0.5 %, standard deviation 0.4 %) during AQABA, yielding that an insignificant amount of NO<sub>2</sub> was lost by conversion to HNO<sub>3</sub> and most NO<sub>2</sub> was converted to ozone during AQABA. We have added a statement on page 12, line 274 following: Here we assumed that all NO<sub>2</sub> formed via reactions R4 and R5 is photolyzed and converted to ozone.
- 15 This is justified by the finding that the noontime ratio  $(k_{\text{NO}_2+\text{OH}}[\text{NO}_2][\text{OH}]) / (j(\text{NO}_2)[\text{NO}_2])$  varied between 0 and 1 % (average 0.5 %, standard deviation 0.4 %) during AQABA, yielding that an insignificant amount of NO<sub>2</sub> was lost by conversion to HNO<sub>3</sub> and most NO<sub>2</sub> was converted to ozone during AQABA.
- 20 We have further corrected the numeration of Reactions R12 and R13 to R10 and R11, respectively, and accordingly changed the respective reaction reference in the text on page 12, line 287 and 288.

# Net ozone production and its relationship to NO<sub>x</sub> and VOCs in the marine boundary layer around the Arabian Peninsula

Ivan Tadic<sup>1</sup>, John N. Crowley<sup>1</sup>, Dirk Dienhart<sup>1</sup>, Philipp Eger<sup>1</sup>, Hartwig Harder<sup>1</sup>, Bettina Hottmann<sup>1</sup>,  
25 Monica Martinez<sup>1</sup>, Uwe Parchatka<sup>1</sup>, Jean-Daniel Paris<sup>2</sup>, Andrea Pozzer<sup>1,4</sup>, Roland Rohloff<sup>1</sup>, Jan  
Schuladen<sup>1</sup>, Justin Shenolikar<sup>1</sup>, Sebastian Tauer<sup>1</sup>, Jos Lelieveld<sup>1,3</sup>, and Horst Fischer<sup>1</sup>

<sup>1</sup>Atmospheric Chemistry Department, Max Planck Institute for Chemistry, Mainz, Germany

<sup>2</sup>Laboratoire des Sciences du Climat et de l'Environnement, LSCE/IPSL, CEA-CNRS-UVSQ, Université Paris-Saclay, Gif-sur-Yvette, France

30 <sup>3</sup>Energy, Environment and Water Research Center, The Cyprus Institute, Nicosia, Cyprus

<sup>4</sup>International Centre for Theoretical Physics, Trieste, Italy

*Correspondence to:* Ivan Tadic (i.tadic@mpic.de)

**Abstract.** Strongly enhanced tropospheric ozone mixing ratios have been reported in the Arabian Basin, a region with intense solar radiation and high concentrations of ozone precursors such as nitrogen oxides and volatile organic compounds. To  
35 analyze photochemical ozone production in the marine boundary layer (MBL) around the Arabian Peninsula, we use ship-borne observations of NO, NO<sub>2</sub>, O<sub>3</sub>, OH, HO<sub>2</sub>, HCHO, actinic flux, water vapor, pressure and temperature obtained during the summer 2017 Air Quality and Climate in the Arabian Basin (AQABA) campaign, compare them to simulation results of the ECHAM-MESSy atmospheric chemistry (EMAC) general circulation model. Net ozone production rates (NOPR) were greatest with 16 ppb<sub>v</sub> day<sup>-1</sup> over both the Gulf of Oman and the Northern Red Sea and with 32 ppb<sub>v</sub> day<sup>-1</sup> over the Arabian  
40 Gulf. NOPR over the Mediterranean, the Southern Red Sea and the Arabian Sea did not significantly deviate from zero; however, results for the Arabian Sea indicate weak net ozone production of 5 ppb<sub>v</sub> day<sup>-1</sup>, and net ozone destruction over the Mediterranean and the Southern Red Sea with -1 ppb<sub>v</sub> day<sup>-1</sup> and -4 ppb<sub>v</sub> day<sup>-1</sup>, respectively. Constrained by HCHO/NO<sub>2</sub>-ratios, our photochemistry calculations show that net ozone production in the MBL around the Arabian Peninsula occurs mostly in NO<sub>x</sub>-limitation regimes with a significant share of ozone production occurring in the transition regime between NO<sub>x</sub>- and  
45 VOC-limitation over the Mediterranean and more significantly over the Northern Red Sea and Oman Gulf.

## 1 Introduction

Revenues from exploitation of the great oil reserves in the states of and around the Arabian Peninsula have propelled remarkable economic development associated with industrialization and urbanization. Strong population growth and anthropogenic emissions of gases and particulates in the last few decades have resulted in the Middle East becoming a hotspot for air pollution and associated health effects, while it is also one of the regions worldwide where climate change is particularly rapid (Lelieveld et al., 2016a). Unique meteorological conditions such as intense solar radiation, high temperatures and aridity, as well as strong anthropogenic emissions of volatile organic compounds (VOCs) and  $\text{NO}_x$  ( $= \text{NO} + \text{NO}_2$ ) by on- and off-shore petrochemical industries, dense ship traffic, fossil energy production for air conditioning and desalination, and urban development are expected to further intensify in the future and contribute to photochemical ozone production (Lelieveld et al., 2009; Krotkov et al., 2016; Pfannerstill et al., 2019). Understanding the sources and sinks of  $\text{NO}_x$  and other ozone precursors on and around the Arabian Peninsula is therefore of major importance for atmospheric chemistry studies, including the investigation of net ozone production rates (NOPR) (Monks et al., 2015; Reed et al., 2016; Bozem et al., 2017).

$\text{NO}_x$  plays a central role in atmospheric photochemistry (Nakamura et al., 2003; Tuzson et al., 2013; Reed et al., 2016). It is the primary precursor for tropospheric ozone ( $\text{O}_3$ ), secondary organic aerosols and photochemical smog in urban areas (Hollaway et al., 2012; Javed et al., 2019). Main ground-based sources of  $\text{NO}$  and  $\text{NO}_2$  are fossil fuel combustion and to a lesser extent bacterial processes in soils, and both lightning and aircraft emissions in the upper troposphere (Nakamura et al., 2003; Miyazaki et al., 2017; Javed et al., 2019). Transport of  $\text{NO}_x$  in the atmosphere is relatively limited due to its short lifetime of a few hours (Reed et al., 2016). It is removed from the troposphere mainly by conversion to  $\text{HNO}_3$  (via reaction with  $\text{OH}$ ) during the day, or the formation of  $\text{N}_2\text{O}_5$  (in the reaction of  $\text{NO}_2$  with  $\text{NO}_3$  at night-time), which also leads to formation of nitric acid by heterogeneous hydrolysis on aerosol surfaces (Crutzen, 1973; Liu et al., 2016; Reed et al., 2016). Ultimately, the deposition of  $\text{HNO}_3$  constitutes the major loss process of  $\text{NO}_x$  from the atmosphere. Ozone is a secondary pollutant that is photochemically formed in the troposphere from its precursors  $\text{NO}_x$  and VOCs (Bozem et al., 2017; Jaffe et al., 2018). It is an important greenhouse gas, an atmospheric oxidant and the most important primary precursor for  $\text{OH}$  (Lelieveld et al., 2004; Monks et al., 2015; Bozem et al., 2017).  $\text{O}_3$  in the planetary boundary layer causes health damage, notably respiratory diseases, and reduces crop yields (Monks et al., 2015; Jaffe et al., 2018).

$\text{NO}_x$  and  $\text{O}_3$  mixing ratios in the troposphere vary from less than 20 ppt<sub>v</sub> and 10 ppb<sub>v</sub>, respectively, for pristine conditions such as the remote marine boundary layer (MBL) up to mixing ratios of several hundreds of ppb<sub>v</sub> in regions with heavy automobile traffic and in international shipping lanes (for  $\text{NO}_x$ ) and downwind of urbanized areas (for  $\text{O}_3$ ) (Reed et al., 2016; Jaffe et al., 2018). Low  $\text{NO}_x$  environments such as the clean MBL and the lower free troposphere are considered net ozone destruction regimes whereas the upper troposphere and areas with anthropogenic emissions of ozone precursors are regions of net ozone production (Klonecki and Levy, 1997; Bozem et al., 2017). Measurements performed in the Houston Ship Channel revealed NOPR of the order of several tens of ppb h<sup>-1</sup> (Chen et al., 2010; Mao et al., 2010; Ren et al., 2013).

In the last decade much effort has been successfully devoted to the mitigation of NO<sub>x</sub> emissions over Europe and America, and levels of reactive nitrogen trace gases have decreased (Miyazaki et al., 2017). But in Asia, India and the Middle East, NO<sub>x</sub> emissions have substantially increased during the last decade so that the global NO<sub>x</sub> burden has essentially remained constant (Miyazaki et al., 2017). NO<sub>x</sub> emissions by ocean-going vessels have attracted considerable attention as they are reported to account for 15 % of the global NO<sub>x</sub> emission burden (Celik et al., 2019). Model calculations suggest that the Arabian Gulf, with an estimated annual NO<sub>x</sub> emission density of about one ton km<sup>-2</sup> from ship traffic, is among the regions with highest NO<sub>x</sub> emission densities worldwide (Johansson et al., 2017). Although NO<sub>x</sub> emissions in the Red Sea and Arabian Sea areas were reported to be three and five times smaller than for the Arabian Gulf, respectively, these values are still 50-100 times larger than the emission density reported for the South Pacific Ocean, for example (Johansson et al., 2017).

In the present study, we characterize photochemical NOPR in the MBL around the Arabian Peninsula. In Sect. 2, the campaign, instrument description, data processing and a description of the methods used in this study is presented. In Sect. 3, mixing ratios of nitrogen oxides and ozone around the Arabian Peninsula are reported. Based on concurrent measurements of HO<sub>x</sub>, actinic flux, temperature and pressure, noontime (HO<sub>2</sub>+RO<sub>2</sub>) mixing ratios are estimated and used to calculate NOPR in the different regions around the Arabian Peninsula. Observation-based analysis of HCHO/NO<sub>2</sub>-ratios will be used to distinguish between NO<sub>x</sub>- or VOC-limited chemistry in the particular regions. A comparison of the results with data retrieved from the 3D global circulation model EMAC is also included.

## 2 Experimental

### 2.1 AQABA campaign

The AQABA ship campaign (Air Quality and Climate in the Arabian Basin) investigated the chemical composition of the MBL around the Arabian Peninsula. From late June to early September 2017, the *Kommandor Iona* Research and Survey Vessel sailed from Toulon (France) to Kuwait and back in order to perform gas-phase and particle measurements in the region. The gas-phase and aerosol measurement instrumentation was housed in five laboratory containers on the front deck. A 6 m high, 20 cm diameter cylindrical stainless steel common inlet was installed on the front deck of the vessel to sample air at a total mass flow rate of 10,000 SLM. NO and NO<sub>2</sub> chemiluminescence measurements were obtained at a total bypass flow rate of 28.5 SLM sampling air from the common inlet with a residence time in the tubing of ~3 s. HCHO, NO<sub>2</sub> cavity ring-down spectroscopy and O<sub>3</sub> measurements were obtained with similar bypass systems sampling air from the common inlet. H<sub>2</sub>O vapor was measured on the top of the ship mast in the front. The OH and HO<sub>2</sub> detection units were placed on the prow to allow for inlets with residence times less than 10 ms.

The *Kommandor Iona* left Malta in late June 2017 traversing the Mediterranean Basin, the Suez Canal and the Northern Red Sea. A 3 day stop over at KAUST University (Saudi Arabia) was made from 11 July 2017 to 13 July 2017 before passing the Southern Red Sea area. On 17 July 2017, we briefly stopped at Djibouti port before passing the Gulf of Aden, the Arabian Sea

and the Gulf of Oman. Kuwait at the northern end of the Arabian Gulf marked the turning point of the ship cruise where, during a second 3-day stop-over, scientific staff was exchanged. The *Kommandor Iona* started the second leg on 03 August 2017 arriving in Toulon (France) in early September 2017 without any further stops. Figure 1 shows the ship's route subdivided into six different regimes.

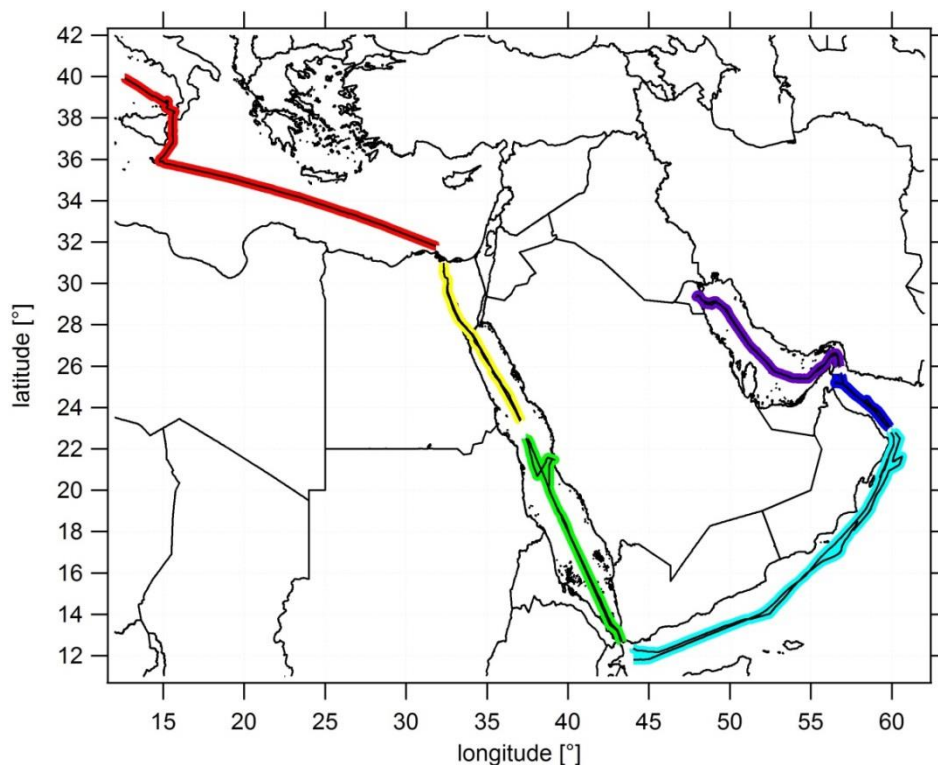


**Figure 1: Ship cruises during both legs and color-coded subdivision into six different regimes. The following abbreviations will be used: AG for Arabian Gulf (purple), OG for Oman Gulf (dark blue), AS for Arabian Sea (blue), SRS for Southern Red Sea (green), NRS for Northern Red Sea (yellow), M for Mediterranean (red).**

To enhance the statistical significance of our results and due to comparable signatures of the  $\text{NO}_x$  and  $\text{O}_3$  measurements in the northern part of the Red Sea, the Suez Gulf and the Suez Canal, we have combined these regions which are represented by the 'Northern Red Sea' (NRS). For the same reasons we have merged the Gulf of Aden with the Arabian Sea (AS). See supplementary Table ST1 for the range of latitudinal and longitudinal coordinates of the different regions and supplementary Table ST2 for a detailed day to day description of the route.

## 2.2 Measurements of nitrogen oxides during AQABA

125 Chemiluminescent detection of NO and NO<sub>2</sub> is a widely applied method to quantify mixing ratios from the ppm<sub>v</sub> down to the  
low ppt<sub>v</sub> range (Nakamura et al., 2003; Pollack et al., 2011; Hosaynali Beygi et al., 2011; Reed et al., 2016). During AQABA  
we deployed a compact, robust and commercially available two-channel chemiluminescence instrument CLD 790 SR (ECO  
Physics AG, Dürnten, Switzerland) that has been optimized for in situ field measurements during the last decade (Hosaynali  
Beygi et al., 2011). The measurement principle of the CLD is based on the addition of O<sub>3</sub> to NO to produce stoichiometric  
130 quantities of excited state NO<sub>2</sub><sup>\*</sup> that will emit an infrared photon ( $\lambda > 600$  nm) forming the chemiluminescent detection  
principle for NO (Drummond et al., 1985; Reed et al., 2016). Both channels feature an identical layout and were operated at a  
mass flow of 1.5 SLM during AQABA. One channel of the CLD (NO<sub>c</sub>-channel) has additionally been equipped with a LED  
solid state photolytic converter (Droplet Measurement Techniques, Boulder, Colorado) installed upstream of the O<sub>3</sub> addition  
to selectively photolyze NO<sub>2</sub> to NO, which is subsequently measured. In this section, we will concentrate on modifications  
135 made prior to the campaign and especially on operational conditions of the photolytic converter during the campaign. Further  
details on the measurement principle are described elsewhere (Pollack et al., 2011; Hosaynali Beygi et al., 2011; Reed et al.,  
2016).

During AQABA, the cylindrical photolytic converter (length 14 cm, volume ~ 0.079 l) was operated at a constant pressure of  
95 hPa yielding a residence time of ~ 0.3 s. The photolytic NO<sub>2</sub> converter features a set of 200 UV LED units attached to each  
140 end of the converter. The emission profile of the UV LED units was characterized in laboratory measurements to peak at 398  
nm with a Full Width at Half Maximum (FWHM) of 16 nm. The UV-induced positive bias in the NO<sub>2</sub>-measurement due to  
photolysis of BrONO<sub>2</sub>, HONO, NO<sub>3</sub> and ClNO<sub>2</sub> to produce NO was estimated at 6.1 %, 2.8 %, 2.7 % and 1.2 %, respectively,  
based on the absorption cross sections from the MPI-Mainz UV/VIS Spectral Atlas of Gaseous Molecules (Keller-Rudek et  
al., 2013). These values represent upper limits for the interference of the respective NO<sub>y</sub> compound as the respective molecular  
145 quantum yield was estimated conservatively at 1. Note that the values represent percent interferences if the interferent had the  
same concentration as NO<sub>2</sub>. Due to small daytime concentrations of these molecules in the MBL, a UV-induced bias was  
neglected for the observations in this study. To limit wall loss of NO<sub>2</sub>, the inner cavity surface is made of PTFE  
(polytetrafluoroethylene), which may potentially provide a reservoir (via surface adsorption) for NO<sub>y</sub> that can thermally  
dissociate to increase the background signal of the NO<sub>2</sub> measurement (Reed et al., 2016). The conversion efficiency  $K_e$  of the  
150 photolytic NO<sub>2</sub> conversion was estimated by gas phase titration (SYCOS K-GPT-DLR, ansyco, Karlsruhe, Germany) several  
times before, during and after the campaign at  $(29.4 \pm 0.9) \%$  allowing the calculation of NO<sub>2</sub> concentrations by  $[\text{NO}_2] =$   
 $\frac{[\text{NO}_c] - [\text{NO}]}{K_e}$ . To avoid chemical interferences due to adding ozone in excess during a gas phase titration, a small but not vanishing  
amount of NO has always been left unoxidized during gas phase titrations.

During AQABA, regular dry zero-air measurements as well as NO and NO<sub>2</sub> calibrations were performed autonomously over a 10 minute period every 6 hours to accurately quantify the instrumental background and to correct for sensitivity drifts. An autonomous cycle of ‘2 min zero air measurements – 2 min NO calibration – 2 min zero air measurement – 2 min NO<sub>2</sub> calibration – 2 min zero air measurement’ was implemented. Continuous flows NO and NO<sub>2</sub> calibration gases were added to the synthetic airflow or directed to a pump by switching solenoid valves. The NO calibration standard ( $1.954 \pm 0.039$  ppm<sub>v</sub> NO in N<sub>2</sub>, Air Liquide, Germany) used during the campaign was compared to a primary standard ( $5.004 \pm 0.025$ ) ppm<sub>v</sub> (NPL, Teddington, UK) after the campaign yielding an effective NO mixing ratio of ( $2.060 \pm 0.057$ ) ppm<sub>v</sub> in the NO calibration gas. Zero air measurements and NO calibrations were performed with a total flow of 3.44 SLM achieving an overflow of 0.44 SLM to guarantee ambient air free standard measurements. The calibration gas was added at 4.5 sccm to the zero air flow. During AQABA, NO calibrations at 2.5 ppb<sub>v</sub> were achieved. During the first leg of the campaign, zero air was sampled from a bottle (Westfalen AG, Germany), whereas during the second leg zero air was generated from a zero air generator (Air Purifier CAP 180, aCuraLine). Zero air measurements generated with the zero air generator were statistically not significantly different from those achieved by a bottle. To correctly account for the photomultiplier background and chemical interferences due to reactions of ozone with ambient alkenes additional pre-chamber measurements were performed every 5 minutes as well as at the beginning of zero air measurements and calibrations for 25 s each. This correction is removing a large fraction of the interference signal from alkenes. However, in regions where alkene concentrations are strongly varying in time and magnitude, the CLD is prone to enhanced backgrounds due to the interference of alkenes with ozone in the instrument. A schematic setup of the two-channel CLD instrument is given in Figure 2.

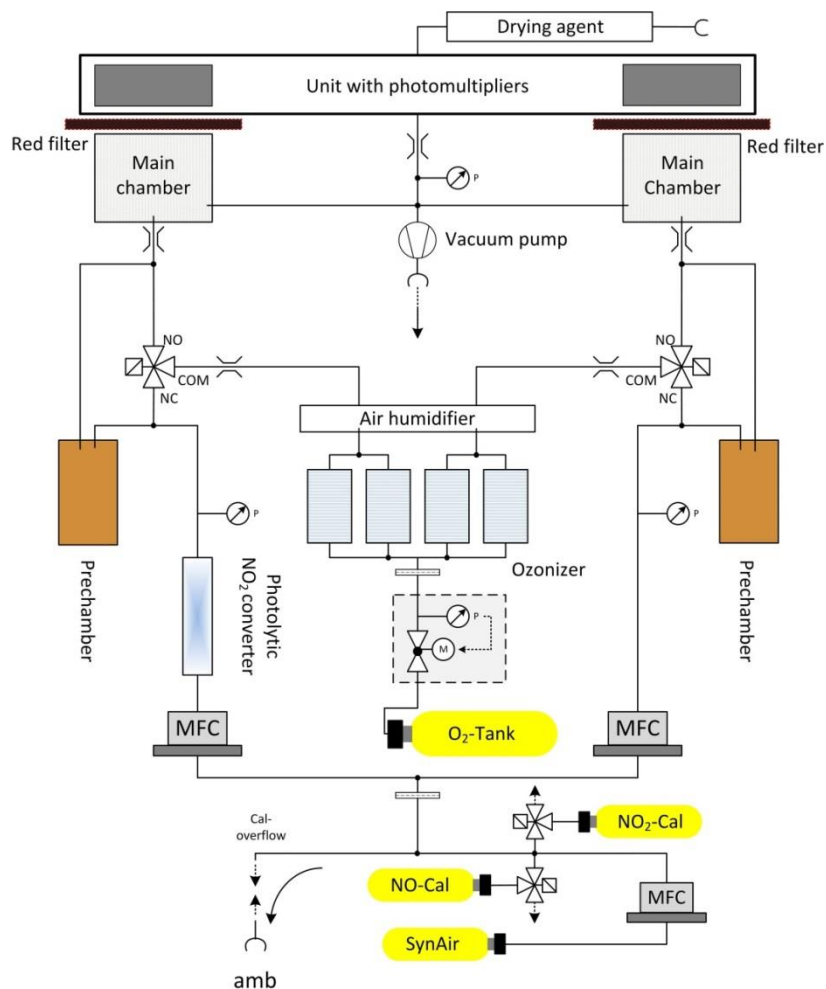


**Figure 2: Schematic setup of the two channel CLD instrument in the configuration used during AQABA. NO and NO<sub>2</sub> calibration gases were running continuously and were added to the zero airflow by switching the respective solenoid valves.**

The total measurement uncertainty (TMU) in NO has been calculated at 6 % at an integration time of 5 minutes and a confidence level of  $1\sigma$  by adding the precision (5 %) and the error of the calibration gas mixture (3 %) in quadrature:

$TMU([NO]) = \sqrt{(5\%)^2 + (3\%)^2} \approx 6\%$ . Note that the precision is calculated from the reproducibility of all in-field calibrations, which is mainly determined by drifts in the detector sensitivity rather than by statistical Poisson noise of the measured signal.

The limit of detection in the NO channel was estimated as the full width at half maximum of the frequency distribution of all zero air measurements obtained during the campaign to be 9 ppt<sub>v</sub> at a 5 min integration time and a confidence level of  $1\sigma$ . The TMU for NO<sub>2</sub> has been estimated as the largest error possible of the statistically dependent variables NO and NO<sub>c</sub>.



$$\text{TMU}([\text{NO}_2]) = \frac{1}{[\text{NO}_2]} \cdot \left( \left| \frac{\Delta[\text{NO}_c]}{K_e} \right| + \left| \frac{\Delta[\text{NO}]}{K_e} \right| + \left| \frac{\Delta K_e \cdot ([\text{NO}_c] - [\text{NO}])}{K_e^2} \right| \right)$$

185 Note that the total measurement uncertainty of the  $\text{NO}_c$ -channel data has also been calculated at 6 % at an integration time of 5 minutes and a confidence level of  $1\sigma$  by adding the precision and the error of the calibration gas mixture in quadrature. Over the course of the campaign the median and the average relative uncertainty of  $\text{NO}_2$  are 13 % and 23 %, respectively. The relative uncertainty in  $\text{NO}_2$  has been estimated as a conservative upper limit at 23 % as the average of the relative uncertainties of all data points obtained during AQABA. As the zero air measurements in the  $\text{NO}_2$  channel produced an increased background affected by memory effects after exposure to high  $\text{NO}_x$  levels e.g. during measurements of stack emissions, the  $\text{NO}_2$  raw data were initially processed without converter background subtraction. As we therefore expect the CLD  $\text{NO}_2$  data to be offset due to not being initially background corrected, the converter background was estimated at 112 ppt<sub>v</sub> from the centre of a Gaussian fit representing the difference of 1-minute averaged CLD  $\text{NO}_2$  and concurrent cavity ring-down spectroscopy (CRDS)  $\text{NO}_2$  measurements for data points below 10 ppb<sub>v</sub>. Setting the threshold for calculating the difference of the two concurrent data sets to 10 ppb<sub>v</sub> is somewhat arbitrary, however, changing this limit to 5 ppb<sub>v</sub> or 20 ppb<sub>v</sub> does not significantly vary the estimated offset of the CLD  $\text{NO}_2$  data. The offset correction of 112 ppt<sub>v</sub> was taken as the ultimate absolute measurement uncertainty of the CLD  $\text{NO}_2$  measurement. Further corrections of to the final CLD data include residence time corrections as well as corrections for NO and  $\text{O}_3$  losses and the subsequent formation of  $\text{NO}_2$  in the sampling line (Ryerson et al., 2000). Both NO and  $\text{NO}_2$  CLD data have also been corrected for nonlinearities for concentrations higher than 55 ppb<sub>v</sub>, as experienced during probing of stack emissions.

### 2.3 Further measurements used in this study

An extensive set of concurrent measurements providing mixing ratios of  $\text{O}_3$ ,  $\text{NO}_2$ , HCHO, OH,  $\text{HO}_2$ , absolute humidity and actinic flux, temperature and pressure data obtained during AQABA was used in this study. Ozone was measured with an absorption photometer (Model 202 Ozone Monitor, 2B Technologies, Boulder, Colorado) based on the well-established absorption of the mercury line in the Hartley band at 254 nm (Viallon et al., 2015). Eliminating water and particle interferences during sampling was achieved via sampling through a nafion tube and a Teflon filter. The ozone monitor was zeroed ten times during the campaign.  $\text{NO}_2$  was further measured by cavity ring-down spectroscopy (Sobanski et al., 2016) and used for correcting the instrumental background of the CLD  $\text{NO}_2$  data, as described above (the correction was taken as the ultimate absolute measurement uncertainty in the CLD  $\text{NO}_2$  data). Note that in this study we will use the  $\text{NO}_2$  CLD data rather than the  $\text{NO}_2$  CRDS data as the temporal coverage of the CLD  $\text{NO}_2$  data over the course of the campaign is about 60 % compared to about 35 % for the cavity ring-down measurement. Formaldehyde (HCHO) was measured with an Aerolaser 4021 (AEROLASER GmbH, Garmisch-Partenkirchen, Germany), which is a fully automatized monitor based on the Hantzsch technique (Kormann et al., 2003).  $\text{H}_2\text{O}$  measurements were obtained using a cavity ring-down spectroscopy monitor (PICARRO G2401, Santa Clara, California) supervised by Laboratoire des Sciences du Climat et de l'Environnement (LSCE) (Kwok et al., 2015).

215 Measurements of OH and HO<sub>2</sub> were performed with the custom-built HydrOxyl Radical measurement Unit based on  
fluorescence Spectroscopy (HORUS) instrument based on laser-induced fluorescence (LIF) spectroscopy of the OH molecule  
and NO titration of HO<sub>2</sub> to OH followed by LIF spectroscopy detection of the OH molecule (Martinez et al., 2010; Regelin et  
al., 2013). HO<sub>2</sub> data used in this study is still preliminary due to not yet corrected interference of organic peroxy radicals RO<sub>2</sub>.  
The largest uncertainty due to interference by contribution of RO<sub>2</sub> is 7 % or 3 ppt<sub>v</sub>, whichever is higher. The 1 sigma accuracy  
220 of both OH and HO<sub>2</sub> is 20 %. The uncertainty in the OH data is here estimated as the 1 sigma accuracy of the data set at 20 %,  
whereas the uncertainty in HO<sub>2</sub> is estimated at  $\sqrt{20\%^2 + 7\%^2} \approx 21\%$ . As HO<sub>2</sub> data are preliminary in this study, they will  
be called HO<sub>2</sub>\*. Wavelength resolved down-welling actinic flux was measured with a spectral radiometer (model CCD  
Spectroradiometer 85237). The *j*-values for NO<sub>2</sub> and O<sub>3</sub> were not corrected for upwelling UV radiation and were estimated to  
have a ~ 10 % measurement uncertainty (Meusel et al., 2016). The radiometer was installed 10 m above sea level, respectively  
225 5 m above the front deck surface. Decreases in sensitivity due to sensor contamination with e.g. sea-spray were corrected with  
a linear interpolation between two (daily) cleaning events. Temperature and pressure measurements were performed with the  
Shipborne European Common Automatic Weather Station (EUCAWS), a weather station specifically designed for ships. The  
weather station incorporates sensors, processing units, satellite positioning and communication systems in one device and is  
implemented and coordinated by the European National Meteorological Service EUMETNET. Table 1 lists the measurement  
230 methods and the TMU for each observation.

**Table 1: List of observations and gas phase measurements during AQABA. The relative uncertainty associated with each data set is given. Note that for OH and HO<sub>2</sub>\*, the relative uncertainty is estimated as the 1 $\sigma$  accuracy (and the 7 % interference of RO<sub>2</sub> in the case of HO<sub>2</sub>\* data). In addition, a reference of the measurement operability are given.**

Molecule	Method	Associated relative uncertainty	References
NO	chemiluminescence	6 %	Hosaynali Beygi et al., 2011
NO <sub>2</sub>	photolysis-chemiluminescence	23 %	Hosaynali Beygi et al., 2011
NO <sub>2</sub>	cavity ring-down spectroscopy	7 %	Sobanski et al., 2016
O <sub>3</sub>	UV absorbance	2 %	Viallon et al., 2015
OH	LIF	20 %	Martinez et al., 2010
HO <sub>2</sub> *	NO titration / LIF	21 %	Martinez et al., 2010
HCHO	Hantzsch technique	13 %	Kormann et al., 2003
H <sub>2</sub> O	cavity ring-down spectroscopy	5 %	Kwok et al., 2015
actinic flux	spectral radiometer	10 %	Meusel et al., 2016

235 The *Kommandor Iona* Research and Survey Vessel sailed whenever possible with the wind coming from the bow to avoid contamination by stack emissions. However, based on the relative wind direction, the variability in NO as well as the temporal evolution of NO<sub>x</sub>, SO<sub>2</sub>, and O<sub>3</sub> sections of data in which the air mass was contaminated by the ship's stack were identified. All data used here to calculate (HO<sub>2</sub>+RO<sub>2</sub>) and NOPR have been filtered to remove contaminated air masses. Altogether, 21 % of the sampling time was potentially contaminated by the ship exhaust of the KI of which 87 % occurred on the first leg. During  
240 the second leg the ship sailed against the wind and most of the data was free of stack contamination. Our analysis is based on a 5-minute running mean for each data set, whereby only averages that have been calculated at a temporal coverage greater than 30 % have been used. A time series of the NO, NO<sub>2</sub> (both CLD), O<sub>3</sub>, OH, HO<sub>2</sub>\* and j(NO<sub>2</sub>) measurements is given in the supplementary Figures S2 and S3.

NO and NO<sub>2</sub> were measured from 03 July 2017 to 31 August 2017, O<sub>3</sub> was measured from 22 June 2017 to 01 September  
245 2017, HCHO from 01 July 2017 to 31 August 2017 and OH and HO<sub>2</sub>\* from 18 July 2017 to 31 August 2017. For the analysis of peroxy radicals RO<sub>2</sub> and NOPR around the Arabian Peninsula we have removed data measured during the stop-overs in Jeddah (11 July to 13 July), Kuwait (31 July to 03 August) and during bunkering at Fujairah City (06 August, 07:00 – 15:00 UTC). Due to HO<sub>x</sub> data being available from 18 July 2017 onward, we have limited the net ozone production analysis to the period after this date.

250

## 2.4 Methods

The so-called NO<sub>x</sub>-O<sub>3</sub>-null cycle represents a rapid daytime cycling between NO, NO<sub>2</sub> and O<sub>3</sub>. Solar UV radiation photolyzes NO<sub>2</sub> to NO and O(<sup>3</sup>P) (R1) which will reform O<sub>3</sub> in the subsequent reaction with molecular oxygen O<sub>2</sub> (R2) (Leighton, 1961). NO and O<sub>3</sub> react to form NO<sub>2</sub> and O<sub>2</sub> (R3). R1, R2 and R3 constitute a so called null cycle which establishes photostationary  
255 steady state (PSS) for both NO<sub>x</sub> and O<sub>3</sub> in mid latitudes during noon time on a time scale of ~100 s (Thornton et al., 2002; Mannschreck et al., 2004).



260 Under the assumption of PSS, the Leighton Ratio  $\varphi$  is unity (Leighton, 1961)

$$\varphi = \frac{j(\text{NO}_2) \cdot [\text{NO}_2]}{k_{\text{NO}+\text{O}_3} \cdot [\text{NO}][\text{O}_3]} = 1 \quad (1)$$

with  $j(\text{NO}_2)$  being the  $\text{NO}_2$  photolysis rate [ $\text{s}^{-1}$ ]. In low  $\text{NO}_x$  environments ( $< 100 \text{ ppt}_v$ ) previous studies have indicated that further  $\text{NO}$  oxidizing trace gases such as peroxy radicals ( $\text{HO}_2$ ,  $\text{RO}_2$ ) and halogen monoxides ( $\text{XO}$ ) may result in a deviation from unity (Nakamura et al., 2003; Hosaynali Beygi et al., 2011; Reed et al., 2016).



Deviations from expected  $\text{NO}/\text{NO}_2$ -ratios at low  $\text{NO}_x$  generally refer to missing oxidants converting  $\text{NO}$  to  $\text{NO}_2$  (Hosaynali Beygi et al., 2011; Reed et al., 2016) or to a measurement error due to an instrumental background or a positive interference from thermal labile  $\text{NO}_x$  reservoir species (Reed et al., 2016; Silvern et al., 2018). In the present study we include  $\text{HO}_2$  and  $\text{R}_i\text{O}_2$  into the production term for  $\text{NO}_2$ .

270

$$j(\text{NO}_2) \cdot [\text{NO}_2] = k_{\text{NO}+\text{O}_3} \cdot [\text{NO}][\text{O}_3] + k_{\text{NO}+\text{HO}_2} \cdot [\text{NO}][\text{HO}_2] + [\text{NO}] \cdot \sum_i k_{\text{NO}+\text{R}_i\text{O}_2} \cdot [\text{R}_i\text{O}_2] \quad (2)$$

Assuming that the temperature-dependent rate coefficient for the reaction of each particular peroxy radical  $\text{R}_i\text{O}_2$  with  $\text{NO}$  equals the rate  $k_{\text{NO}+\text{HO}_2}$  for Reaction R4 (Hauglustaine et al., 1996; Cantrell et al., 1997; Thornton et al., 2002), we can combine the sum of all organic peroxy radicals  $\text{R}_i\text{O}_2$  to the entity  $\text{RO}_2$ . The sum of  $\text{HO}_2$  and  $\text{RO}_2$  can be estimated using the steady state equation

275

$$[\text{HO}_2] + [\text{RO}_2] = \frac{j(\text{NO}_2) \cdot [\text{NO}_2] - k_{\text{NO}+\text{O}_3} \cdot [\text{NO}][\text{O}_3]}{k_{\text{NO}+\text{HO}_2} \cdot [\text{NO}]} \quad (3)$$

However, the steady state assumption is not valid if the sampled air parcel is affected by fresh emissions or fast changes in the actinic flux (Thornton et al., 2002). After sampling a fresh emission e.g. a ship plume, for which  $\text{NO}_x$  went up typically to values of several tens of  $\text{ppb}_v$  with simultaneous titration in  $\text{O}_3$ , we assume that PSS is re-established on a time scale of 2 minutes (Thornton et al., 2002; Mannschreck et al., 2004). To best approximate PSS in our analysis we have restricted the estimation of  $\text{RO}_2$  on time frames  $\pm 2 \text{ h}$  around noontime for which we expect the smallest relative changes in the actinic flux. Noontime for each day was determined as the centre of a Gaussian fit that was applied to the actinic flux data. We applied a Gaussian Fit to the actinic flux data as this fitting method is sufficient to estimate the centre of the diurnal actinic flux. To further limit the effect of periods for which PSS is not fulfilled, we use the median instead of the average that is often disproportionately biased by strong  $\text{NO}_x$  sources nearby. See supplementary Tables ST3, ST5 and ST7 for detailed statistics and a further motivation on regional averages and median values. See supplementary Figure S1 for a detailed illustration of the calculation of the fraction of the noontime integral.

285

A further part of the analysis will be the investigation of NOPR. Ozone production is initiated by reactions that produce HO<sub>x</sub>,  
 290 for which primary production is from the photolysis of ozone, formaldehyde, nitrous acid (HONO) and hydrogen peroxide  
 (H<sub>2</sub>O<sub>2</sub>) (Thornton et al., 2002; Lu et al., 2010; Hens et al., 2014; Mallik et al., 2018). The production of ozone can be  
 approximated by the rate of oxidation of NO with HO<sub>2</sub> and RO<sub>2</sub> to form NO<sub>2</sub> that will rapidly form O<sub>3</sub> (R1-R2) (Parrish et al.,  
 1986; Thornton et al., 2002; Bozem et al., 2017).

$$P(O_3) = k_{NO+HO_2}[NO] \cdot ([HO_2] + [RO_2]) \quad (4)$$

295 Here we assumed that all NO<sub>2</sub> formed via reactions R4 and R5 is photolyzed and converted to ozone. This is justified by the  
 finding that the noontime ratio  $(k_{NO_2+OH}[NO_2][OH]) / (j(NO_2)[NO_2])$  varied between 0 and 1 % (average 0.5 %, standard  
 deviation 0.4 %) during AQABA, yielding that an insignificant amount of NO<sub>2</sub> was lost by conversion to HNO<sub>3</sub> and most NO<sub>2</sub>  
 was converted to ozone during AQABA. Photochemical O<sub>3</sub> loss is mainly due to photolysis ( $\lambda < 340$  nm) in the presence of  
 water vapor and the reactions of ozone with OH and HO<sub>2</sub> (Bozem et al., 2017).



$\alpha$ , the fraction of O(<sup>1</sup>D) that reacts with H<sub>2</sub>O

$$305 \quad \alpha = \frac{k_{O(^1D)+H_2O}[H_2O]}{k_{O(^1D)+H_2O}[H_2O] + k_{O(^1D)+M}[M]} \quad (5)$$

was  $(10.6 \pm 2.2)$  % during AQABA with a quasi linear dependence on water concentrations. The error in  $\alpha$  is mainly  
 determined by the error of H<sub>2</sub>O at 5 %. Furthermore, ozone is lost due to reactions with alkenes (R10) and halogen radicals  
 (R11).



We find that the loss rate is dominated by the photolysis of ozone with subsequent reaction of O(<sup>1</sup>D) with H<sub>2</sub>O, was 60 – 80  
 % of the total loss rate, followed by the reaction of O<sub>3</sub> with HO<sub>2</sub>, which makes up 10 – 30 % (note that the uncertainty in HO<sub>2</sub>  
 radical concentrations mentioned above has no significant influence on the total O<sub>3</sub> loss rate, due to its small contribution).  
 The remaining fraction (10-30 %) is due to the reaction of O<sub>3</sub> with OH. The reaction of ozone with ethene is on average 0.005  
 315 – 0.01 ppbv h<sup>-1</sup> and therefore generally less than 2 % of the total ozone loss rate (Bourtsoukidis et al., 2019). The reaction of  
 O<sub>3</sub> with all alkenes will hence be neglected. Halogen radicals were not measured during AQABA and will not be incorporated

into our study. Based on oxidative pairs, Bourtsoukidis et al. (2019) have classified the majority of their samples collected during AQABA by an OH/Cl-ratio of 200:1. As measured daytime OH concentrations were of the order of  $5 \cdot 10^6$  molecule  $\text{cm}^{-3}$ , the estimate would yield a Cl concentration of  $2.5 \cdot 10^4$  molecule  $\text{cm}^{-3}$ , which would decrease the estimated diurnal net ozone production rates by roughly 0.2 ppb<sub>v</sub> day<sup>-1</sup> over the Arabian Sea and at most 0.6 ppb<sub>v</sub> day<sup>-1</sup> over the other regions, which does not substantially alter the here presented results. The noontime chemical ozone loss rate can be summarized by

$$L(\text{O}_3) = [\text{O}_3] \cdot (\alpha \cdot j(\text{O}^1\text{D}) + k_{\text{OH}+\text{O}_3} \cdot [\text{OH}] + k_{\text{HO}_2+\text{O}_3} \cdot [\text{HO}_2]). \quad (6)$$

NOPR presented in this study is finally calculated as the difference of Eq. 4 and Eq. 6.

$$\text{NOPR} = k_{\text{NO}+\text{HO}_2} [\text{NO}] \cdot ([\text{HO}_2] + [\text{RO}_2]) - [\text{O}_3] \cdot (\alpha \cdot j(\text{O}^1\text{D}) + k_{\text{OH}+\text{O}_3} [\text{OH}] + k_{\text{HO}_2+\text{O}_3} [\text{HO}_2]) \quad (7)$$

Under the assumption of constant chemical composition for a given day, the NOPR is expected to have a diel cycle following the measured actinic flux. Hence integrating the estimated NOPR over the course of a day based on the particular fractional noontime integral of  $j(\text{NO}_2)$  will yield a diurnal value for NOPR. A detailed calculation of the diurnal fractional integrals is given in the supplementary Figure S1. Note that all reaction rate constants used are from the IUPAC Task Force on Atmospheric Chemistry Chemical Kinetic Data Evaluation (Atkinson et al., 2004). Indications whether a chemical regime is NO<sub>x</sub>-limited or VOC-limited can be derived from the ratio of HCHO to NO<sub>2</sub>. Former studies have derived HCHO/NO<sub>2</sub>-ratios from satellite measurements to establish whether ozone production is NO<sub>x</sub>-limited or VOCs-limited. The results indicate NO<sub>x</sub>-limitation for HCHO/NO<sub>2</sub> > 2 and prevailing VOC-limitation for HCHO/NO<sub>2</sub> < 1 (Duncan et al., 2010).

## 2.5 ECHAM/MESSy Atmospheric Chemistry (EMAC) model

EMAC is a 3D general circulation model that includes a variety of sub-models to describe numerous processes in the troposphere, their interaction with oceans and land surfaces and incorporates anthropogenic influences. Here we use the second development cycle of the Modular Earth Submodel System (MESSy2) (Jöckel et al., 2010) and ECHAM5 (Röckner et al., 2006) which is the fifth generation European Centre Hamburg general circulation model in the T106L31 resolution (corresponding to a quadratic grid of roughly 1.1° and 1.1°). The model has 31 vertical pressure levels and involves the complex organic chemistry mechanism MOM (Mainz Organic Mechanism) as presented by Sander et al. (2019) that includes further developments of the version used by Lelieveld et al. (2016b). Here we use the lowest pressure level in a terrain following coordinates (equivalent to the surface level) and simulations of NO, NO<sub>2</sub>, O<sub>3</sub>, OH, HO<sub>2</sub>,  $j(\text{NO}_2)$  and  $j(\text{O}^1\text{D})$ . The sum of peroxy radicals was estimated as the sum of all radicals R<sub>i</sub>O<sub>2</sub> with less than four carbon atoms. Net ozone production based on data retrieved from EMAC was estimated as

$$\text{NOPR} = [\text{NO}] \cdot (k_{\text{NO}+\text{HO}_2} [\text{HO}_2] + \sum_i k_{\text{NO}+\text{R}_i\text{O}_2} [\text{R}_i\text{O}_2]) - [\text{O}_3] \cdot (\alpha \cdot j(\text{O}^1\text{D}) + k_{\text{OH}+\text{O}_3} [\text{OH}] + k_{\text{HO}_2+\text{O}_3} [\text{HO}_2]). \quad (8)$$

A list of all included peroxy radicals R<sub>i</sub>O<sub>2</sub> for the reaction with NO is given in the supplementary Table ST10.

### 3 Results and discussions

#### 3.1 NO<sub>x</sub> and O<sub>3</sub> in the MBL around the Arabian Peninsula

During AQABA NO<sub>x</sub> mixing ratios varied over three orders of magnitude with lowest values of less than 50 ppt<sub>v</sub> observed in relatively pristine regions and highest values of more than 10 ppb<sub>v</sub> found in the vicinity of areas with strong anthropogenic influence or nearby passing ships. Ozone mixing ratios ranged from values of less than 20 ppb<sub>v</sub>, detected over the Arabian Sea, to more than 150 ppb<sub>v</sub> during episodes of severe pollution. Figures 3a) and 3b) show distributions of NO<sub>x</sub> measured during the first and second leg of the campaign (range from 0.1 ppb<sub>v</sub> to 20 ppb<sub>v</sub>) while Figure 3c) and 3d) show corresponding ozone mixing ratios covering a range from 20 ppb<sub>v</sub> to 100 ppb<sub>v</sub>, respectively. A classification of the different regions based on Box-Whisker-Plots, including the 25-75-percentile interval (box) and whiskers for the 10-90-percentile interval, is shown in Figure 4 and Figure 5 for NO<sub>x</sub> and O<sub>3</sub>, respectively. As average NO<sub>x</sub> is often influenced by fresh, localized emissions, we have included the median (black bar) instead of the average in the Box-Whisker-Plot for NO<sub>x</sub>, which is less sensitive to extreme values. For O<sub>3</sub>, although the difference between median and mean is mostly negligible, we also use the median in Figure 5. NO<sub>x</sub> and O<sub>3</sub> averages, medians, standard deviations, 1<sup>st</sup> and 3<sup>rd</sup> quantiles and the number of data points quantified per region are given in the supplementary Table ST3. See supplementary Figure S4 for OH and HO<sub>2</sub>\* mixing ratios around the Arabian Peninsula. Supplementary Figure S5 shows that absolute humidity observed during AQABA ranges from lowest values of less than 1 % observed in the Suez Golf during the first leg to about 3 % observed during both legs in the southeastern part of the Arabian Gulf and in the Strait of Hormuz. Although observing highest absolute humidity on both legs in the southeastern part of the Arabian Gulf, absolute humidity was very low on the first leg near Kuwait, where absolute humidity was about 1 %. These air masses were brought from the Kuwait/Iraq area into the MBL of the Arabian Gulf on the first leg, whereas a change of wind direction for the second leg resulted in winds coming from Iran area with moister air. For the rest of the cruise, absolute humidity mixing ratio was about 1.5 % with variations being generally less than 0.5 %.

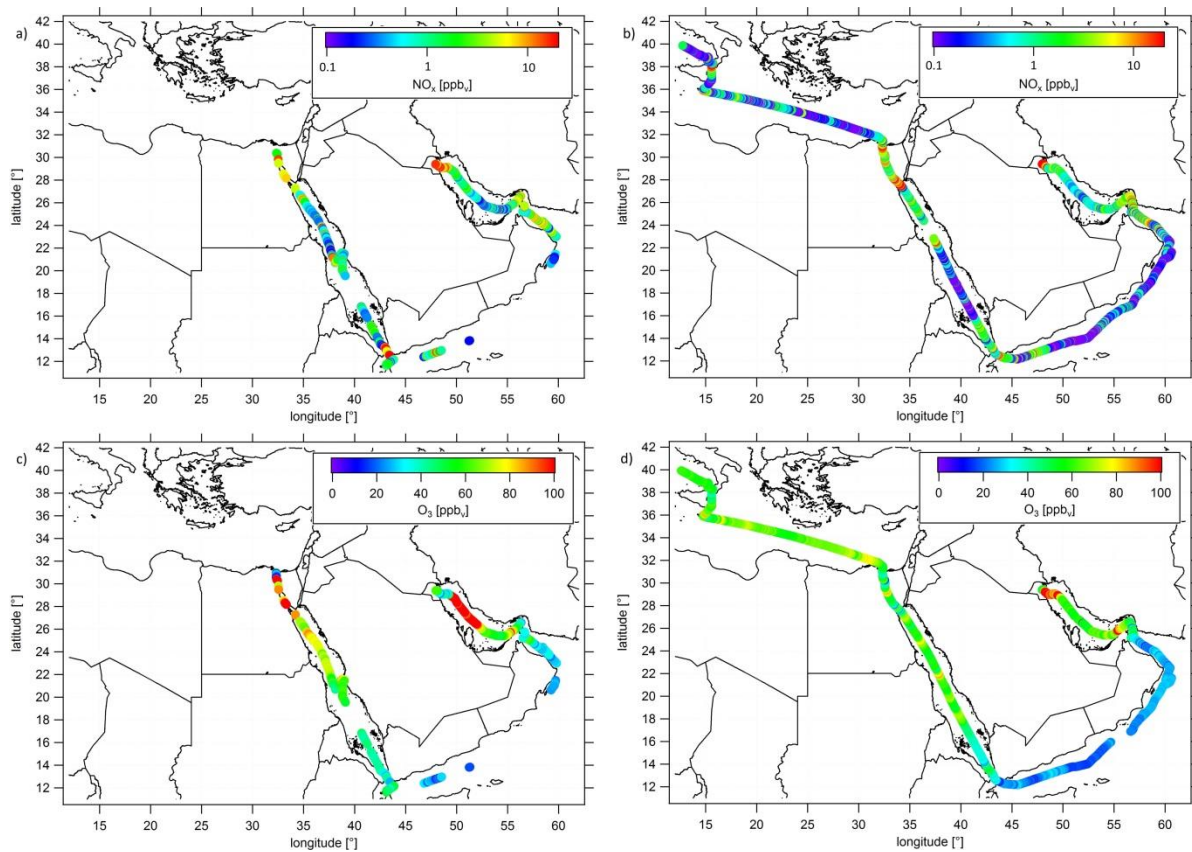


**Figure 3: Ship cruises with color-scaled NO<sub>x</sub> mixing ratios (logarithmic scale) a) during the first and b) the second leg and color-scaled O<sub>3</sub> mixing ratios (linear scale) c) during the first and d) during the second leg. Note that both NO<sub>x</sub> and O<sub>3</sub> has been filtered for own stack contamination.**



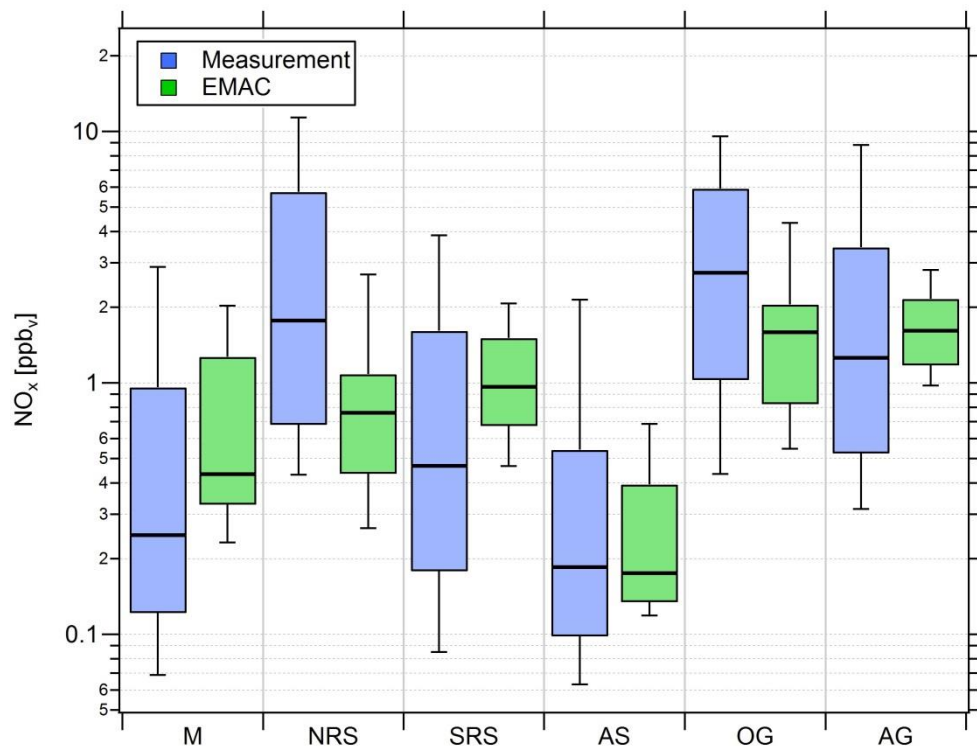
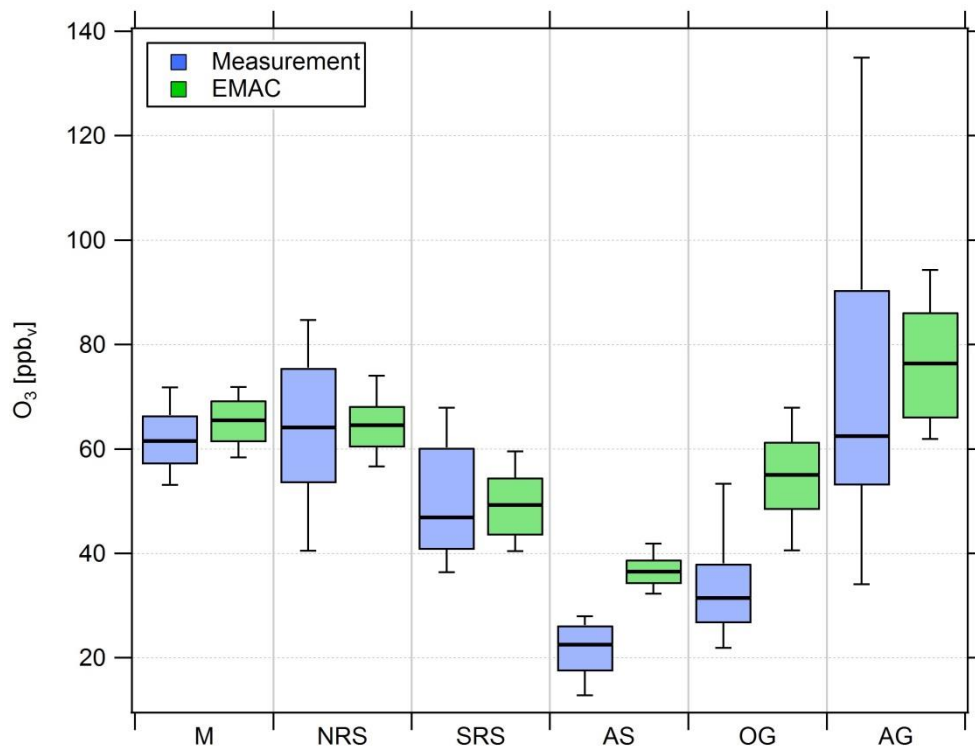


Figure 4: Comparison of measured (blue) and simulated (green)  $\text{NO}_x$  mixing ratios in the six different regions investigated during AQABA. The horizontal black bar indicates the median value, the box the 25- and 75-percentiles and the whiskers the 10- and 90-percentiles.



**Figure 5: Comparison of measured (blue) and simulated (green)  $O_3$  mixing ratios in the six different regions investigated during AQABA. The horizontal black bar indicates the median value, the box the 25- and 75-percentiles and the whiskers the 10- and 90-percentiles.**

Overall, we find that  $NO_x$  mixing ratios over the Northern Red Sea, the Gulf of Oman and the Arabian Gulf are approximately one order of magnitude higher than in the other three regions (Southern Red Sea, Arabian Sea, Mediterranean).  $NO_x$  medians over the Arabian Gulf, the Northern Red Sea and the Gulf of Oman are 1.26 ppbv, 1.76 ppbv and 2.74 ppbv, respectively. Lower median  $NO_x$  mixing ratios were measured over the Southern Red Sea (0.46 ppbv), the Mediterranean (0.25 ppbv) and the Arabian Sea (0.19 ppbv). With respect to observed  $O_3$  mixing ratios, the Arabian Sea is the only region representing remote MBL conditions with lowest median and average  $O_3$  of 21.5 ppbv and 22.5 ppbv, respectively, followed by the Gulf of Oman where median and mean  $O_3$  were 31.5 ppbv and 34 ppbv, respectively. The low  $O_3$  mixing ratios over the Arabian Sea were accompanied by the smallest variability (whisker-interval: 15.1 ppbv). Although observing highest  $NO_x$  over the Oman Gulf,  $O_3$  observed over the Oman Gulf was amongst the lowest detected throughout the whole campaign, which can partly be explained the fact that high  $NO_x$  eventually leads to ozone destruction. The immediate vicinity of point sources in this region, which leads to higher  $NO_x$  (before it is lost by reaction with OH and deposition to the surface) and titration of  $O_3$  (note the relatively low regional  $O_3$  median of 31.5 ppbv), may partly explain why  $NO_x$  was highest over the Gulf of Oman. However, a significantly larger whisker-interval of observed ozone of 31.4 ppbv over the Gulf of Oman indicates increasing amounts of pollution and advection from the Arabian Gulf where extreme events of ozone were observed several times during the

395 campaign with maximum mixing ratios of up to 170 ppb<sub>v</sub> when wind was coming from Kuwait/Iraq. Please note that during the second leg wind was coming from Iran (Pfannerstill et al., 2019). The whisker-interval over the Arabian Gulf was 100.9 ppb<sub>v</sub>, more than six times higher than that over the Arabian Sea. Reasons for large variations of both NO<sub>x</sub> and O<sub>3</sub> over the Arabian Gulf were a multitude of point sources as well as a change in the observed wind direction with air masses coming from Iraq/Kuwait area during the first leg and air masses coming from Iran during the second leg (Pfannerstill et al., 2019).  
400 Over the Mediterranean, the Northern Red Sea and the Southern Red Sea, median ozone was 61.5 ppb<sub>v</sub>, 64.2 ppb<sub>v</sub> and 46.9 ppb<sub>v</sub>, respectively. The whisker-intervals over the Northern Red Sea and the Southern Red Sea were 44.2 ppb<sub>v</sub> and 31.6 ppb<sub>v</sub>, respectively. Air masses over the Mediterranean were characterized as photochemically aged due to their impact by northerly winds (Etesians) which bring processed/oxidized air from eastern Europe (Turkey, Greece) to the Mediterranean area (Derstroff et al., 2017; Pfannerstill et al., 2019). This photochemical ageing/oxidation over the Mediterranean leads to a rather  
405 small whisker-interval of 18.7 ppb<sub>v</sub> in ozone. In summary, median NO<sub>x</sub> over the Oman Gulf was 56 % and 117 % higher than over the Northern Red Sea and the Arabian Gulf, respectively. However, the highest NO<sub>x</sub> average was measured over the Northern Red Sea at 4.69 ppb<sub>v</sub>, similar to the values observed over the Oman Gulf (4.16 ppb<sub>v</sub>) and the Arabian Gulf (3.65 ppb<sub>v</sub>). Note that highest NO<sub>x</sub> mixing ratios over the Oman Gulf and over the Northern Red Sea are not always associated with high O<sub>3</sub> mixing ratios. We find that average ozone was highest over the Arabian Gulf with 74 ppb<sub>v</sub> followed by the Northern  
410 Red Sea region (63.4 ppb<sub>v</sub>). The average ozone mixing ratio over the Oman Gulf was 34 ppb<sub>v</sub>, which corresponds to 46 % of the value observed over the Arabian Gulf. Photochemically aged air masses over the Mediterranean Basin show an ozone average of 61.6 ppb<sub>v</sub> and air masses encountered over the Northern Red Sea (O<sub>3</sub> median of 64.2 ppb<sub>v</sub>, O<sub>3</sub> average of 63.4 ppb<sub>v</sub>) are comparable to the Arabian Gulf.

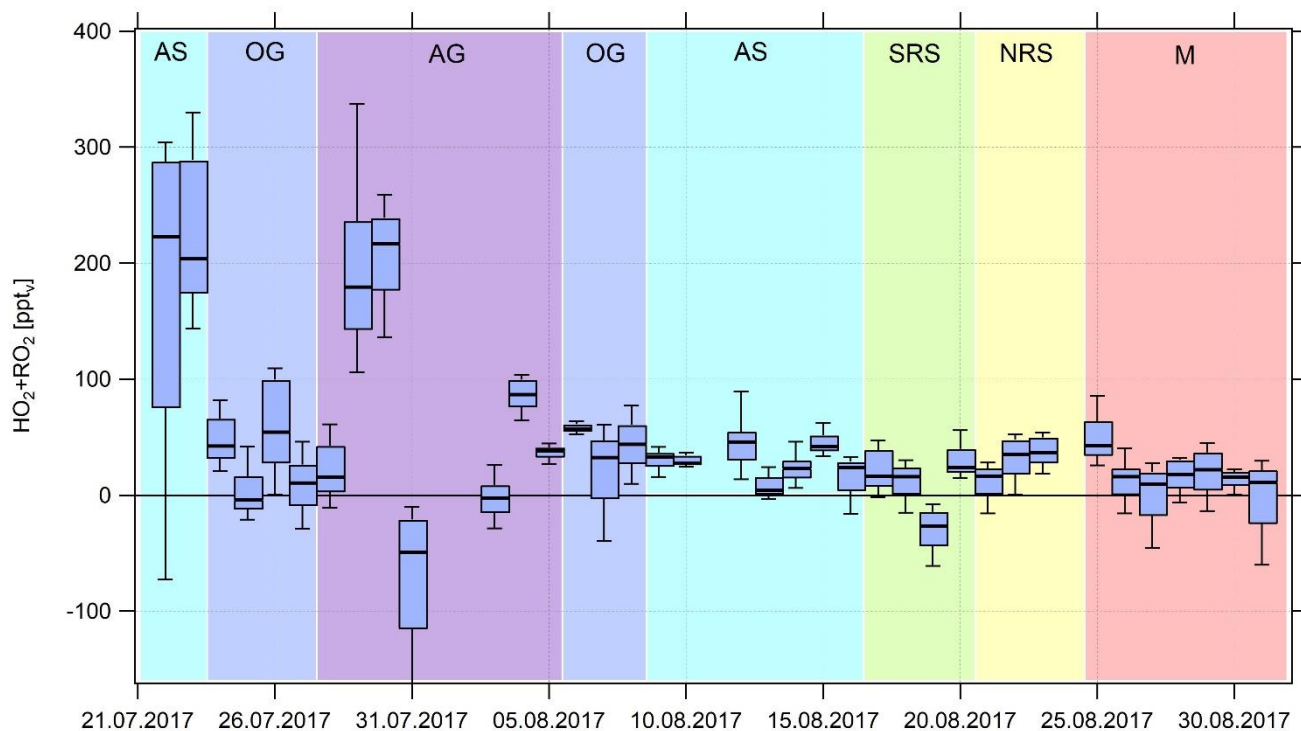
Due to a number of large pollution sources in the region around the Arabian Peninsula such as passing ships, highly urbanized  
415 areas as well as on- and off-shore petrochemical processing, NO<sub>x</sub> levels were rarely as low as those found in remote locations such as over the South Atlantic (Fischer et al., 2015) where NO<sub>x</sub> levels may be under 20 ppt<sub>v</sub>. Apart for a few occasions where NO<sub>x</sub> was below 50 ppt<sub>v</sub> for short periods (Arabian Sea, the Southern Red Sea and the Mediterranean), NO<sub>x</sub> levels during AQABA generally ranged from 100 ppt<sub>v</sub> up to several ppb<sub>v</sub>. The campaign NO<sub>x</sub> median of 0.65 ppb<sub>v</sub> and mean value of (2.51 ± 5.84) ppb<sub>v</sub> is comparable to urban sites (Kleinman et al., 2005). A detailed emission density analysis performed by Johansson  
420 et al. (2017) shows that NO<sub>x</sub> emissions on and around the Arabian Peninsula are amongst the highest worldwide, which could explain the rather high NO<sub>x</sub> level in the MBL around the peninsula (Johansson et al., 2017; Pfannerstill et al., 2019). O<sub>3</sub> mixing ratios measured during AQABA were also very variable with O<sub>3</sub> mixing ratios ranging between less than 20 ppb<sub>v</sub> in the remote MBL (Fischer et al., 2015) to 60-70 ppb<sub>v</sub> in the Mediterranean (consistent with previous ship-based measurements in the region (Kouvarakis et al., 2002) and as high as 150 ppb<sub>v</sub> measured over the Arabian Gulf region. The latter are consistent with O<sub>3</sub>  
425 mixing ratios reported from regions influenced by oil and gas processing (Pfannerstill et al., 2019) and shipping lanes such as the Houston Ship Channel (Mazzuca et al., 2016).

Figure 4 also shows that the general trend for NO<sub>x</sub> mixing ratios in the different regions is widely reproduced by the EMAC model. We find that the median NO<sub>x</sub>(model)/NO<sub>x</sub>(measurement)-ratio of all five minute averaged data points of the whole campaign is 0.91, indicating that the model underestimates NO<sub>x</sub> by roughly 10 %. The average ratio and its standard deviation are significantly larger at 2.57 and 5.71, respectively, indicating that single modeled data points strongly exceed the measurements, especially during periods of low in situ NO<sub>x</sub> (see supplementary Figure S6). Particularly over the Arabian Sea and the Southern Red Sea, the model generally simulates NO<sub>x</sub> mixing ratios higher than 100 and 200 ppt<sub>v</sub>, respectively while the measurements indicate mixing ratios of less than 50 ppt<sub>v</sub> for certain periods. Furthermore, as expected, the model is not able to reproduce point sources such as passing ships for which we observe a significant underestimation of the measured NO<sub>x</sub>.

For ozone we find that the median O<sub>3</sub>(model)/O<sub>3</sub>(measurement)-ratio throughout the campaign is 1.23, indicating that over the course of the campaign the model overestimates O<sub>3</sub> by about 23 %. This could partly be related to the same limitation, i.e. the inability of the model to resolve point sources in which O<sub>3</sub> is locally reduced due to titration by NO. While the model is in rather good agreement with the measurements over the Mediterranean, the Northern Red Sea and Southern Red Sea, large deviations are found over the Arabian Sea and the Oman Gulf, where the model overestimation with respect to the regional median is 63 % and 75 %, respectively. A possible explanation for the overestimation of both ozone and NO<sub>x</sub> in pristine regions such as over the Arabian Sea and the Oman Gulf could be related to the model resolution of 1.1° x 1.1°. Interpolation of model simulations along the *Kommandor Iona* ship track close to the coast at this resolution will most likely incorporate contributions from nearby land areas, affected by anthropogenic emissions. See supplementary Table ST3 and Table ST4 for further information and Figure S6 and S7 for additional scatterplots of measured and simulated regional median NO<sub>x</sub> and O<sub>3</sub>, respectively.

### 3.2 Estimation of (HO<sub>2</sub>+RO<sub>2</sub>) around the Arabian Peninsula

Noontime (HO<sub>2</sub>+RO<sub>2</sub>) was estimated based on Eq. 3. As the steady state assumption will not hold for air masses originating from fresh emissions (times to acquire steady state estimated from the inverse sum of the loss and production terms for NO<sub>2</sub> typically ranged from 1-2 minutes during AQABA) and for fast changes in the actinic flux, we have calculated Box-Whisker-Plots for ± 2 h around noontime for which we expect relatively minor changes in the actinic flux (Figure 6). The noontime of each day was approximated by applying a Gaussian fit routine to the measured  $j(\text{NO}_2)$  values whereas  $j(\text{NO}_2)$  values being less than 10<sup>-3</sup> s<sup>-1</sup> were neglected. Due to the availability of OH and HO<sub>2</sub>\* data from 18 July 2017 onwards, we have limited the analysis to this period. Note that there are no noontime (HO<sub>2</sub>+RO<sub>2</sub>) estimates from 18 July to 21 July due to contamination by the ship exhaust and on 24 August 2017 due to missing data. The black bar in Figure 6 indicates the median value, with the Box-interval marking the 25- and 75-percentile and the whisker showing the 10- and 90-percentile. Figure 7 shows summarized regional trends of the (HO<sub>2</sub>+RO<sub>2</sub>) estimates for measured and simulated data.



**Figure 6: Timeline of median (HO<sub>2</sub>+RO<sub>2</sub>) noontime estimates from 22 July to 31 August 2017. Due to contamination by the ship exhaust itself, there is no data from 18 July to 21 July 2017. See annotations for the classification of the different regions.**

460

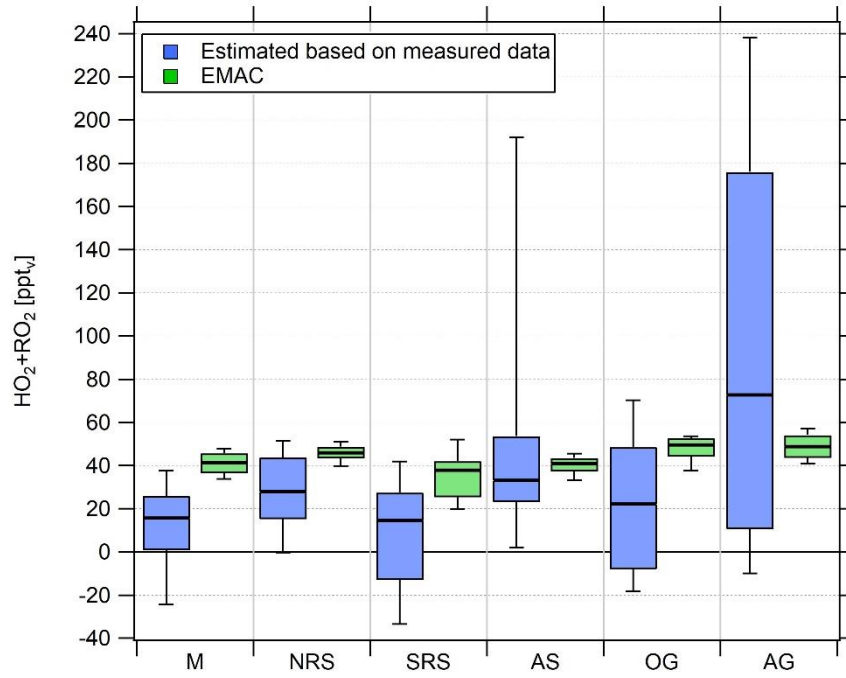


**Figure 7: Comparison of Box-Whisker-Plots of the regional estimated noontime ( $\text{HO}_2+\text{RO}_2$ ) median based on measured data and simulated ( $\text{HO}_2+\text{RO}_2$ ) data for the period from 18 July 2017 onwards.**

465 The relative uncertainty  $R([\text{HO}_2] + [\text{RO}_2])$  associated with the ( $\text{HO}_2+\text{RO}_2$ ) estimate has been calculated by error propagation of Eq. 3.

$$R([\text{HO}_2] + [\text{RO}_2]) = \frac{1}{[\text{HO}_2] + [\text{RO}_2]} \cdot \sqrt{\left( \frac{(\Delta j(\text{NO}_2) \cdot [\text{NO}_2])^2}{k_{\text{NO}+\text{HO}_2} \cdot [\text{NO}]} + \frac{(\Delta [\text{NO}_2] \cdot j(\text{NO}_2))^2}{k_{\text{NO}+\text{HO}_2} \cdot [\text{NO}]} + \frac{(\Delta [\text{O}_3] \cdot k_{\text{NO}+\text{O}_3} \cdot [\text{NO}])^2}{k_{\text{NO}+\text{HO}_2} \cdot [\text{NO}]} + \left( \Delta [\text{NO}] \left( \frac{-k_{\text{NO}+\text{O}_3} \cdot [\text{O}_3] \cdot k_{\text{NO}+\text{HO}_2} \cdot [\text{NO}] - k_{\text{NO}+\text{HO}_2} \cdot (j(\text{NO}_2) \cdot [\text{NO}_2] - k_{\text{NO}+\text{O}_3} \cdot [\text{O}_3] \cdot [\text{NO}])}{(k_{\text{NO}+\text{HO}_2} \cdot [\text{NO}])^2} \right) \right)^2 \right)}$$

Over the course of the campaign, the median relative ( $\text{HO}_2+\text{RO}_2$ ) uncertainty is 74 %. The average is 176 % and heavily biased by single data outliers and therefore not representative. The relative error associated with the ( $\text{HO}_2+\text{RO}_2$ ) calculation is hence estimated at 74 %. Note that our calculation assumes that errors in the used rate coefficients are negligible.

We find median noontime ( $\text{HO}_2+\text{RO}_2$ ) mixing ratios over the Mediterranean, the Northern Red Sea, the Southern Red Sea, the Arabian Sea and Oman Gulf of 16 ppt<sub>v</sub>, 28 ppt<sub>v</sub>, 15 ppt<sub>v</sub>, 33 ppt<sub>v</sub> and 22 ppt<sub>v</sub>, respectively, with each respective 75-percentile  $\text{RO}_2$  being equal or less than 54 ppt<sub>v</sub>. Only over the Arabian Gulf, the  $\text{RO}_2$  estimate yields a median noontime mixing ratio of

475 73 ppt<sub>v</sub> accompanied by the largest variations in the box-interval of the whole campaign. While the box-interval of the (HO<sub>2</sub>+RO<sub>2</sub>) estimate in the other regions is 25-57 ppt<sub>v</sub>, the box-interval over the Arabian Gulf is significantly higher at 165 ppt<sub>v</sub>. Negative values for all regions are regularly found in the vicinity of fresh emissions and air masses not in photochemical equilibrium. The elevated 90-percentile over the Arabian Sea is due to high (HO<sub>2</sub>+RO<sub>2</sub>) estimates during the first leg on 22 and 23 July.

480 Estimated (HO<sub>2</sub>+RO<sub>2</sub>) mixing ratios based on measured tracer data are in general agreement with previous studies performed in marine boundary layer environments which report maximum mixing ratios between 30 and 55 ppt<sub>v</sub> around noontime (Hernandez et al., 2001). As peroxy radicals are short-lived molecules generated from the oxidation of VOCs, enhanced (HO<sub>2</sub>+RO<sub>2</sub>) concentrations observed over the Arabian Gulf are most likely due to high VOC emissions from intense oil and gas activities in the region (Bourtsoukidis et al., 2019; Pfannerstill et al., 2019). However high HO<sub>2</sub> and RO<sub>2</sub> can also occur in  
485 aged air masses with low NO<sub>x</sub> and VOCs but still significant O<sub>3</sub> (and perhaps HCHO whose photolysis would then yield peroxy radicals). Bourtsoukidis et al. report that spatial volume mixing ratios of ethane and propane over the Arabian Gulf were about a factor of 10-15 times higher than over the Arabian Sea and the Southern Red Sea (Bourtsoukidis et al., 2019). We find that the median noontime (HO<sub>2</sub>+RO<sub>2</sub>)(measurement estimate)/HO<sub>2</sub>(measurement)-ratio throughout the whole campaign is 1.88. Note that during single days, HO<sub>2</sub> may be higher than the (HO<sub>2</sub>+RO<sub>2</sub>) estimate, which is within the uncertainty of the  
490 (HO<sub>2</sub>+RO<sub>2</sub>) estimate.

EMAC modelled, median noontime (HO<sub>2</sub>+RO<sub>2</sub>) mixing ratios estimated as the sum of simulated HO<sub>2</sub> and all simulated peroxy radicals with less than four carbon molecules are 41 ppt<sub>v</sub>, 46 ppt<sub>v</sub>, 38 ppt<sub>v</sub>, 41 ppt<sub>v</sub>, 50 ppt<sub>v</sub> and 49 ppt<sub>v</sub> over the Mediterranean, the Northern Red Sea, the Southern Red Sea, the Arabian Sea, the Oman Gulf and the Arabian Gulf, respectively. The observation based (HO<sub>2</sub>+RO<sub>2</sub>) estimate yields 16 ppt<sub>v</sub>, 28 ppt<sub>v</sub>, 15 ppt<sub>v</sub>, 33 ppt<sub>v</sub>, 22 ppt<sub>v</sub> and 73 ppt<sub>v</sub> respectively. We find that  
495 the median point by point (HO<sub>2</sub>+RO<sub>2</sub>)(model)/(HO<sub>2</sub>+RO<sub>2</sub>)(measurement estimate)-ratio from 18 July onward is 1.05 so that, on average, the model overestimates the measurement by 5 %. Please note that the observational variability is much higher than the modeled one and that the median of 1.05 is accompanied by a larger average (1.84) and a large variability (42.51). See supplementary Table ST5 and ST6 for further information and Figure S8 for an additional scatterplot of measured and simulated regional median (HO<sub>2</sub>+RO<sub>2</sub>).

### 500 3.3 Net ozone production rates around the Arabian Peninsula

In the following, net ozone production rates (at noon) are calculated based on Eq. 7 for the different regions. These noontime values are scaled to diurnal production rates (Figure 8). As photochemical net ozone destruction is in good approximation linear with actinic flux  $j(\text{NO}_2)$  and as on average  $(46.1 \pm 2.8) \%$  of the total  $j(\text{NO}_2)$  occurred  $\pm 2\text{h}$  around noon, the median noontime NOPR estimate was multiplied by  $4/0.461 \approx 8.68$  to obtain a diurnal value. The error in the total actinic flux located  
505  $\pm 2\text{h}$  around noon is estimated from the standard deviation of the best estimate of 0.461 at  $\Delta s \approx 6 \%$ . Due to contamination

by the own ship exhaust and due to the availability of OH and HO<sub>2</sub>\* data only from 18 July 2017 onwards, we have limited the analysis to the period from 22 July 2017 to 31 August 2017. A comparison of NOPR estimated based on measured and simulated data for the different regions is shown in Figure 9. A break-down of the different terms of Eq. 7 in the six regions is included in the supplementary Figures S10-S13.

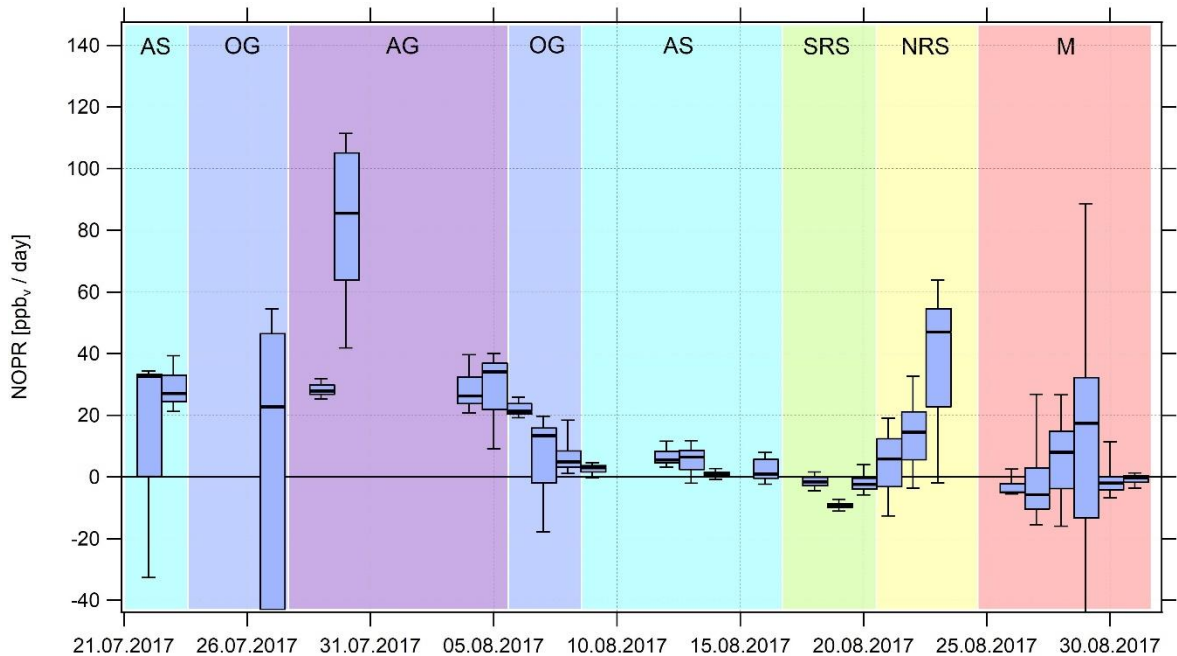


**Figure 8: Timeline of the diurnal NOPR from 22 July to 31 August 2017. NOPR calculations are limited to the time period from 22 July onwards due to missing HO<sub>x</sub> data and contamination by the ship exhaust itself before this period. See annotations for the classification of the different regions.**



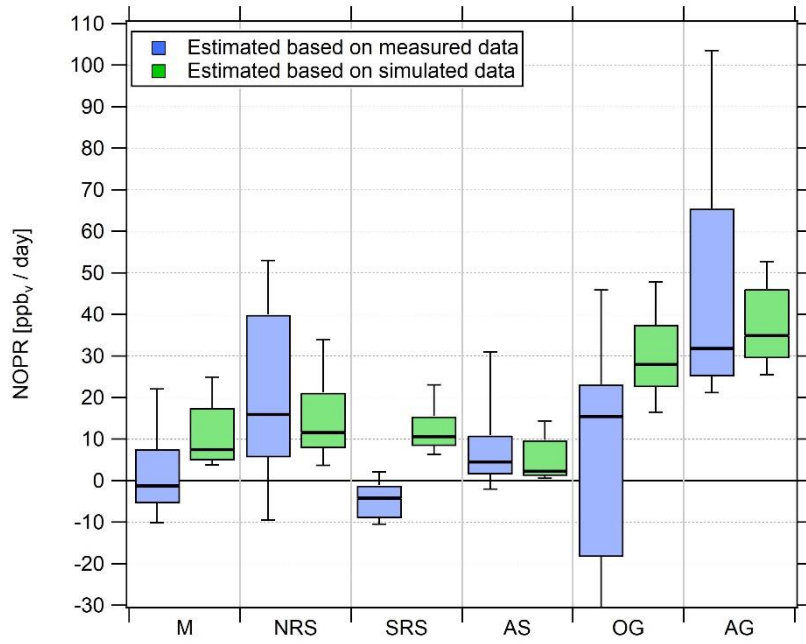


**Figure 9: Diurnal net ozone production rates in the different regions. Related to the magnitude of pollution sources, the lower whisker of the NOPR estimate over the Oman Gulf is -324 ppb day<sup>-1</sup>.**

The relative uncertainty associated with the NOPR estimate has been calculated by error propagation of Eq. 7.

$$R(\text{NOPR}) = \frac{1}{\text{NOPR}} \cdot \sqrt{\left(k_{\text{NO}+\text{HO}_2} \cdot [\text{NO}] \cdot \Delta([\text{HO}_2] + [\text{RO}_2])\right)^2 + \left(k_{\text{NO}+\text{HO}_2} \cdot \Delta[\text{NO}] \cdot ([\text{HO}_2] + [\text{RO}_2])\right)^2 + \left(\Delta[\text{O}_3] \cdot (\alpha \cdot j(\text{O}^1\text{D}) + k_{\text{OH}+\text{O}_3} \cdot [\text{OH}] + k_{\text{HO}_2+\text{O}_3} \cdot [\text{HO}_2])\right)^2 + \left(\Delta j(\text{O}^1\text{D}) \cdot [\text{O}_3] \cdot \alpha\right)^2 + \left(j(\text{O}^1\text{D}) \cdot [\text{O}_3] \cdot \Delta\alpha\right)^2 + \left(\Delta[\text{OH}] \cdot k_{\text{OH}+\text{O}_3} \cdot [\text{O}_3]\right)^2 + \left(\Delta[\text{HO}_2] \cdot k_{\text{HO}_2+\text{O}_3} \cdot [\text{O}_3]\right)^2}$$

Incorporating a relative error of 74 % associated with (HO<sub>2</sub>+RO<sub>2</sub>), the median of the relative NOPR error of all data points obtained during AQABA is 91 %. The average relative uncertainty of NOPR is 21 % and strongly biased by single data outliers, which are in the case of NOPR significantly negative (due to fresh emissions and titration of O<sub>3</sub> by NO). Again the median is a more representative measure for the general uncertainty associated with the NOPR calculations. The relative error associated with the NOPR estimates based on measured data is hence estimated at 91 %.

Over the Mediterranean and the Southern Red Sea, NOPR values do not significantly deviate from zero (production equals loss) within the atmospheric variability. The best estimate indicates slight net ozone destruction for the Mediterranean and Southern Red Sea (- 1 ppb day<sup>-1</sup>) and (- 4 ppb day<sup>-1</sup>) respectively, and slight net production for the Arabian Sea (5 ppb day<sup>-1</sup>), which is significantly positive within the variability of the box-interval. Variations in NOPR calculated as the width of the 25-

75-percentile-box yield comparable values of 9-11 ppb day<sup>-1</sup> for these three regions. Substantial net ozone production was inferred over the Oman Gulf, the Northern Red Sea, and the Arabian Gulf with the median values being 16 ppb day<sup>-1</sup>, 16 ppb day<sup>-1</sup> and 32 ppb day<sup>-1</sup>, respectively. Especially over the Red Sea we find a strong latitudinal gradient in net ozone production rates with higher values towards the northern end, while slight net ozone destruction of -4 ppb day<sup>-1</sup> is reported over the southern part.

NOPR estimates for the Oman Gulf, the Northern Red Sea and the Arabian Gulf are comparable to results reported for dense traffic shipping routes such as the Houston Ship Channel with NOPR of a few tens of ppb h<sup>-1</sup> for periods of severe pollution (Zhou et al., 2014). Similar net ozone production rates have been reported for regions of Beijing in summer 2006 (Lu et al., 2010). For regions with low anthropogenic influence such as the Southern Red Sea and the Arabian Sea we estimate net ozone production that does not differ significantly from zero. This is due to the rather low NO<sub>x</sub> mixing ratios in the clean marine boundary layer (Bozem et al., 2017). Note that we calculated net ozone destruction only for a few days over the Southern Red Sea and the Arabian Sea, indicating that the marine boundary layer around the Arabian Peninsula is rarely free from anthropogenic influence owing to the multitude of on- and off-shore anthropogenic activities.

We find that model-calculated estimates of NOPR reproduce the trends observed for NOPR calculated from in situ measurements except over the Mediterranean and the Southern Red Sea. Although EMAC predicts high ozone levels over the Arabian Sea, it also reports the lowest NOPR in this region. On the other side, the large overestimation of the model-calculated estimate NOPR against the one based on measured tracer data over the Mediterranean and over the Southern Red Sea could be linked to NO<sub>x</sub> being overestimated in the model in these regions. In the model, pollution emissions, especially over the Oman Gulf and the Arabian Gulf, seem to be averaged over a large (1.1° grid size) region. High background concentrations of ozone precursors hence contribute to net ozone production rates that compare to conditions observed in the Houston case (Zhou et al., 2014). Even in the more pristine regions such as over the Southern Red Sea and the Arabian Sea, the model is not able to reproduce net ozone destruction, which is consistent with the fact the ozone is generally too high and that NO<sub>x</sub> levels below 0.1 ppbv are not found in the model. See supplementary Table ST7 and ST8 for further information and supplementary Figure S9 for an additional scatterplot of measured and simulated regional NOPR.

Measured OH and HO<sub>2</sub>\* as well as (HO<sub>2</sub>+RO<sub>2</sub>) estimated based on measured data are generally underestimating the concurrent simulated data. Speaking in terms of absolute amounts, we find that the break-down loss and productions terms of Eq. 7 (NOPR) based on measured data are generally underestimating the results based on simulated data. The deviations between measurement and model pretty much represent the differences observed in the noontime concentrations of the mentioned tracers. Largest deviations of the break-down loss terms, associated with reactions of O<sub>3</sub> with OH and HO<sub>2</sub>, are found over the OG and AG, where also OH and HO<sub>2</sub> is significantly overestimated in the model. In the case of  $j(\text{O}^1\text{D}) \cdot \alpha \cdot [\text{O}_3]$  a slight overestimation by the estimate based on simulated data compared to the estimate based on measured data is observed. This is due to simulated absolute humidity being slightly larger than the concurrent measured data. Also we find that the break-down

production term  $k_{\text{NO}+\text{HO}_2} \cdot [\text{NO}] \cdot ([\text{HO}_2] + [\text{RO}_2])$  estimated based on simulated data is generally larger than the estimate based on measured data. This pretty much reflects that noontime ( $\text{HO}_2+\text{RO}_2$ ) is overestimated in the model by a factor of 2, except for the Arabian Gulf where fair agreement is found.

### 3.4 VOC- and $\text{NO}_x$ -sensitivity

Ozone is photochemically formed when the precursors  $\text{NO}_x$  and VOCs are abundant in the presence of sunlight (Bozem et al., 2017; Jaffe et al., 2018). In order to determine whether a chemical system is  $\text{NO}_x$ - or VOC-limited or in a transition between those two regimes, one has to estimate the total amount of OH reactivity towards VOCs and towards  $\text{NO}_x$ . Therefore the VOC/ $\text{NO}_x$ -ratio is an important indicator of the behavior of  $\text{NO}_x$ , VOCs and  $\text{O}_3$  in a system. Since it is not feasible to precisely define all ambient VOCs (could be thousands), formaldehyde mixing ratios have been used as a proxy for the OH reactivity towards VOCs since it is a short-lived oxidation product of many VOCs that is often positively correlated with peroxy radicals (Sillman et al., 1995; Duncan et al., 2010). Sillman et al. first used afternoon concentrations of indicator species such as HCHO and total reactive nitrogen ( $\text{NO}_y$ ) to determine the sensitivity of ozone production to VOCs or  $\text{NO}_x$  (Sillman et al., 1995). Their approach was later successfully transferred to space-based satellite observations by using the ratio of tropospheric columns of HCHO and  $\text{NO}_2$  to determine the sensitivity of ozone production (Martin et al., 2004). Here we use HCHO/ $\text{NO}_2$ -ratios (referred to as “Ratio”) deduced by Duncan et al. as indicators for the sensitivity of ozone production to  $\text{NO}_x$ - and VOC-limitations in megacities in the United States with large amounts of anthropogenic  $\text{NO}_x$  and VOC emissions (Duncan et al., 2010). The Ratio is an indicator of surface photochemistry as most of the atmospheric column of HCHO and  $\text{NO}_2$  is located in the planetary boundary layer (Duncan et al., 2010). Duncan et al. have derived  $\text{NO}_x$ -limited ozone production regimes for  $\text{HCHO}/\text{NO}_2 > 2$  and VOC-limited ozone production for  $\text{HCHO}/\text{NO}_2 < 1$  (Duncan et al., 2010). For  $1 < \text{HCHO}/\text{NO}_2 < 2$  both  $\text{NO}_x$  and VOC emission reductions may lead to a reduction in ozone. Figure 10 shows the Box-Whisker-Plot classification of the HCHO/ $\text{NO}_2$ -ratio of the different regions during noontime.

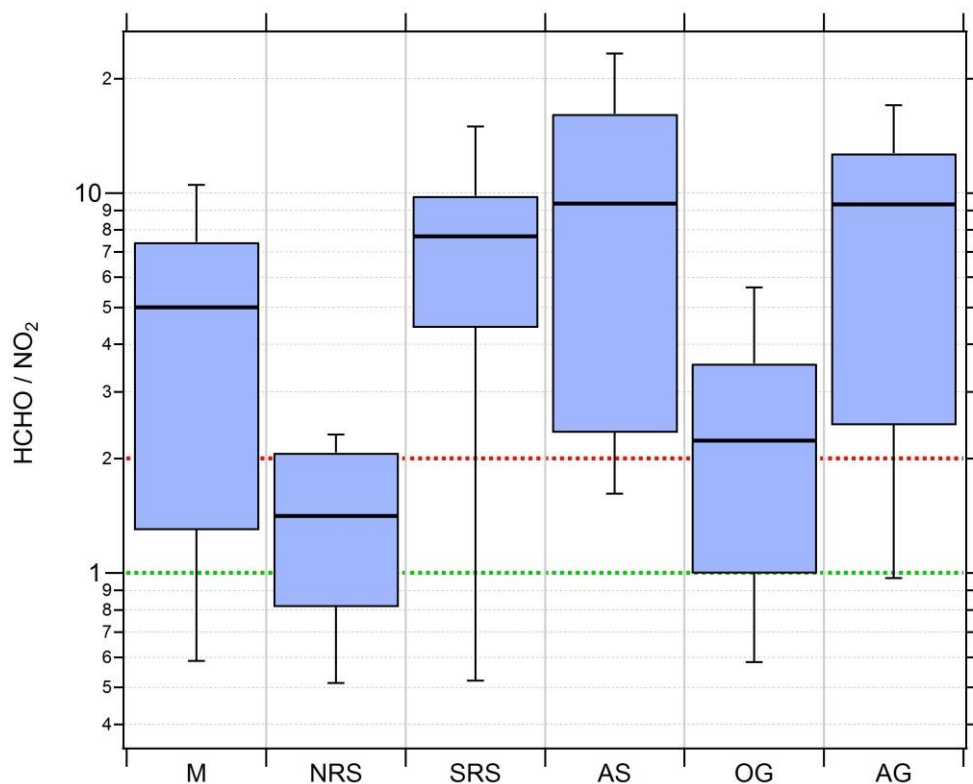


**Figure 10: Box-Whisker-Plots of the HCHO/NO<sub>2</sub>-ratio for the different regions with the black bar indicating the median value. Red (ratio = 2) and green (ratio = 1) lines indicate the limits for HCHO/NO<sub>2</sub> deduced by Duncan et al. (2010) for NO<sub>x</sub>-limitation and VOC-limitation, respectively.**

Median HCHO/NO<sub>2</sub>-ratios of 5, 7.7, 9.4 and 9.3 over the Mediterranean, the Southern Red Sea, the Arabian Sea and the Arabian Gulf respectively indicate tendencies towards NO<sub>x</sub>-limited regimes. In a previous study based on measured OH reactivity, Pfannerstill et al. classified these regions as being mostly in a transition between NO<sub>x</sub>- and VOC-limitation, with a tendency towards NO<sub>x</sub>-limitation (2019). Median HCHO/NO<sub>2</sub>-ratios of 1.4 and 2.2 estimated over the Northern Red Sea and the Oman Gulf signify tendencies towards VOC-limitation. However, none of the medians of the six regions falls below the VOC-limit deduced by Duncan et al. (2010).

Over the Red Sea we find a latitudinal gradient in the HCHO/NO<sub>2</sub>-ratio, similar to the gradients for NO<sub>x</sub> and NOPR. Due to very low NO<sub>x</sub> over the Southern Red Sea, O<sub>3</sub> production is NO<sub>x</sub>-limited, changing into a more VOC-limited regime over the Northern Red Sea. Ozone production over the Mediterranean was classified as rather NO<sub>x</sub>-limited, however partly being in the transition regime between NO<sub>x</sub>- and VOC-limitation, which can be explained by measurements obtained on 29 August 2017 when laying at anchor in front of Malta with a multitude of (NO<sub>x</sub>)-emissions from nearby situated vessels. Average noontime NO<sub>x</sub> on that particular day was about three times as large as the regional average noontime NO<sub>x</sub> observed over the whole

Mediterranean area.  $\text{NO}_x$  limitation is also inferred for the relatively clean Arabian Sea and the polluted Arabian Gulf atmosphere. Note that a further increase in  $\text{NO}_x$ -emissions from shipping in the Arabian Gulf may initially lead to higher ozone production. However, a further increase in  $\text{NO}_x$  might eventually lead to a change from  $\text{NO}_x$ - to VOC-sensitivity and a decrease in ozone production for this region, as observed for the Oman Gulf (median  $\text{HCHO}/\text{NO}_2$ -ratio of 2.2 and average  $\text{O}_3$  of 34 ppb<sub>v</sub>). See supplementary Table ST9 for detailed statistics on regional  $\text{HCHO}/\text{NO}_2$ -ratios.

#### 4 Conclusion

In situ observations of  $\text{NO}$ ,  $\text{NO}_2$ ,  $\text{O}_3$ ,  $\text{HCHO}$ ,  $\text{OH}$ ,  $\text{HO}_2$ , absolute humidity, actinic flux, temperature and pressure were carried out in the marine boundary layer around the Arabian Peninsula during the AQABA ship campaign from late June to early September 2017. Concentration ranges of both  $\text{NO}_x$  and  $\text{O}_3$  clearly showed anthropogenic influence in the MBL.  $\text{NO}_x$  was highest over the Arabian Gulf, the Northern Red Sea and the Oman Gulf. Lowest  $\text{NO}_x$  was observed over the Arabian Sea and over the Southern Red Sea during the second leg.  $\text{O}_3$  mixing ratios were highest over the Arabian Gulf. We observed a latitudinal gradient in  $\text{O}_3$  concentrations with higher values towards the northern part of the Red Sea. Although comparable  $\text{O}_3$  averages were measured over the Northern Red Sea and over the Mediterranean, lower variability over the Mediterranean towards the end of August 2017 indicates photochemically more extensively aged air masses. The lowest regional  $\text{O}_3$  mixing ratio average was detected over the Arabian Sea, which is broadly comparable to remote marine boundary layer conditions in the Northern Hemisphere.

Noontime ( $\text{HO}_2 + \text{RO}_2$ ) estimates based on deviations from the Leighton Ratio yield median values around the Arabian Peninsula amount to 15 – 33 ppt<sub>v</sub> for all regions except over the Arabian Gulf where the median is 73 ppt<sub>v</sub>. The uncertainty due to the missing up-welling actinic flux portion is expected to be insignificant. Furthermore, we estimated noontime and diurnal NOPR based on Eq. 6 and the integral over the actinic flux. Highest diurnal NOPR were observed over the Oman Gulf, the Northern Red Sea and the Arabian Gulf with median values of 16 ppb<sub>v</sub> day<sup>-1</sup>, 16 ppb<sub>v</sub> day<sup>-1</sup> and 32 ppb<sub>v</sub> day<sup>-1</sup>, respectively, which is in agreement with previous studies that predicted net photochemical  $\text{O}_3$  formation conditions in the region. Net ozone destruction was only observed for a few days with clean conditions over the Arabian Sea and the Southern Red Sea. Based on  $\text{HCHO}/\text{NO}_2$ -ratios our analysis suggests tendencies towards  $\text{NO}_x$ -limitation over the Mediterranean, the Southern Red Sea, the Arabian Sea and the Arabian Gulf and VOC-limitation over the Northern Red Sea and the Oman Gulf, which reproduces the trends observed by Pfannerstill et al. (2019).

$\text{NO}_x$  results from the atmospheric chemistry – general circulation model EMAC underestimate the measurement data by 10 % whereas median modeled  $\text{O}_3$  overestimates the measurement by 23 %, the latter being related to limitations in model resolution in coastal proximity and near shipping lanes. Although EMAC generally reproduces regional  $\text{NO}_x$  and  $\text{O}_3$  medians, the scatter when comparing both data sets is large.  $\text{NO}_x$  is generally too low as it does not resolve local point sources and too high for

clean regions. Lowest NO<sub>x</sub> of less than 0.1 ppb<sub>v</sub> found in the in situ measurements is not reproduced by the model as emissions  
635 are averaged over a large area (1.1°). Median noontime (HO<sub>2</sub>+RO<sub>2</sub>) retrieved from the EMAC model are ~ 5 % higher than  
(HO<sub>2</sub>+RO<sub>2</sub>) estimates based on measurement data, however, (HO<sub>2</sub>+RO<sub>2</sub>) deduced from EMAC is sometimes about a factor of  
2 higher than the regional (HO<sub>2</sub>+RO<sub>2</sub>) estimate based on the Leighton Ratio and measured tracer data. NOPR estimates based  
on modeled data reproduce the tendencies derived from the measurements very well. However, the model does not reproduce  
observed net ozone destruction along some clean parts of the ship cruise.

#### 640 **Data availability**

Data used in this study is available to all scientists agreeing to the AQABA protocol at  
<https://doi.org/10.5281/zenodo.3693988>.

#### **Author contributions**

IT, HF and JL designed the study. UP and IT performed the CLD NO and NO<sub>2</sub> measurements and processed the data. JC and  
645 PE performed the O<sub>3</sub> measurements, JS performed the actinic flux measurements. JS performed cavity ring-down spectroscopy  
measurements of NO<sub>2</sub>. DD and BH performed the HCHO measurements. HH, MM, RR, ST performed the OH and HO<sub>2</sub>  
measurements. J-DP was responsible for the H<sub>2</sub>O measurements. Model simulations were made by AP. All authors have  
contributed to writing this manuscript

#### **Competing interests**

650 The authors declare no conflict of interest.

#### **Acknowledgements**

We acknowledge the collaborations with King Abdullah University of Science and Technology (KAUST), The Cyprus  
Institute (CyI) and the Kuwait Institute for Scientific Research (KISR). We would like to thank Marcel Dorf and Claus Koeppel  
for the organization of the campaign. We would like to thank Hays Ships Ltd. and the ship crew for caring about the physical  
655 well-being of the scientific participants and for an unforgettable time on board *Kommandor Iona*. Last but not least we would  
like to thank the whole AQABA community for a successful campaign.

## Appendix: Acronyms and abbreviations

### 660 General

AQABA Air Quality and Climate in the Arabian Basin campaign  
 CyI The Cyprus Institute  
 KAUST King Abdullah University of Science and Technology  
 KISR Kuwait Institute for Scientific Research

### 665 Regions

AG Arabian Gulf  
 AS Arabian Sea  
 M Mediterranean Sea  
 NRS Northern Red Sea  
 670 OG Oman Gulf  
 SRS Southern Red Sea

### Scientific

CLD Chemiluminescence detector  
 CRDS Cavity ring-down spectroscopy  
 675 ECHAM5 Fifth generation European Centre Hamburg general circulation model  
 EMAC ECHAM/MESSy Atmospheric Chemistry model  
 FWHM Full width at half maximum  
 GC-FID Gas chromatography – flame ionization detector  
 HORUS HydOxyl Radical measurement Unit based on fluorescence Spectroscopy instrument  
 680 HO<sub>x</sub> OH + HO<sub>2</sub>  
 LED Light emitting diode  
 LIF Laser induced fluorescence  
 MBL Marine boundary layer  
 MESSy Modular Earth Submodel System  
 685 NOPR Net ozone production rate  
 NO<sub>x</sub> NO + NO<sub>2</sub>  
 PFA Perfluoroalkoxy  
 PSS Photostationary steady state  
 PTFE Polytetrafluoroethylene  
 690 SLM Standard liter per minute  
 STEAM3 Ship Traffic Emission Assessment Model 3  
 TMU Total measurement uncertainty  
 VOC Volatile organic compounds  
 UV Ultraviolet  
 695

## References

- 700 Atkinson, R., Baulch, D. L., Cox, R. A., Crowley, J. N., Hampson, R. F., Hynes, R. G., Jenkin, M. E., Rossi, M. J., and Troe, J.: *Atmos. Chem. Phys.*, 4, 1461, 2004; IUPAC Task Group on Atmospheric Chemical Kinetic Data Evaluation, (<http://iupac.pole-ether.fr>).
- Bourtsoukidis, E., Ernle, L., Crowley, J. N., Lelieveld, J., Paris, J.-D., Pozzer, A., Walter, D., and Williams, J.: Non Methane Hydrocarbon (C2-C8) sources and sinks around the Arabian Peninsula, doi:10.5194/acp-2019-92, 2019.
- 705 Bozem, H., Butler, T.M., Lawrence, M. G., Harder, H., Martinez, M., Kubistin, D., Lelieveld, J., and Fischer, H.: Chemical processes related to net ozone tendencies in the free troposphere, *Atmos. Chem. Phys.*, 17, 10565-10582, doi:10.5194/acp-17-10565-2017, 2017.
- Cantrell, C. A., Shetter, R. E., Calvert, J. G., Eisele, F. L., Williams, E., Baumann, K., William, H. B., Stevens, P. S., Mather, J., H.: Peroxy radicals from photostationary state deviations and steady state calculations during the Tropospheric OH Photochemistry Experiment at Idaho Hill, Colorado, 1993, *J. Geophys. Res.*, 102, 6369-6378, 1997.
- 710 Celik, S., Drewnick, F., Fachinger, F., Brooks, J., Darbyshire, E., Paris, J.-D., Eger, P. G., Schuladen, J., Tadic, I., Friedrich, N., Dienhart, D., Crowley, J. N., Harder, H., and Borrmann, S.: Influence of vessel characteristics and atmospheric processes on the gas and particle phase of ship emission plumes measured in the Mediterranean Sea and around the Arabian Peninsula, *Atmos.- Chem. Phys. Discuss.*, <https://doi.org/10.5194/acp-2019-859>, in review, 2019.
- 715 Chen, S., Ren, X., Mao, J., Chen, Z., Brune, W. H., Lefer, B., Rappenglück, B., Flynn, J., Olson, J., Crawford, J. H.: A comparison of chemical mechanisms based on TRAMP-2006 field data, *Atmos. Environ.*, 44, 4116-4125, doi: 10.1016/j.atmosenv.2009.05.027, 2009.
- Crutzen, P. J.: Photochemical reactions initiated by and influencing ozone in unpolluted tropospheric air, *Tellus*, 26, 47–57, doi:10.1111/j.2153-3490.1974.tb01951.x, 1973.
- 720 Derstroff B., Hüser, I., Bourtsoukidis, E., Crowley, J. N., Fischer, H., Gromov, S., Harder, H., Janssen, R. H. H., Kesselmeier, J., Lelieveld, J., Mallik, C., Martinez, M., Novelli, A., Parchatka, U., Phillips, G. J., Sander, R., Sauvage, C., Schuladen, J., Stönnner, C., Tomsche, L., and Williams, J.: Volatile organic compounds (VOCs) in photochemically aged air from the eastern and western Mediterranean, *Atmos. Chem. Phys.*, 17, 9547-9566, doi:10.5194/acp-17-9547-2017, 2017.



- Duncan, B. N., Yoshida, Y., Olson, J. R., Sillman, S., Martin, R. V., Lamsal, L., Hu, Y., Pickering, K. E., Retscher, C., Allen, D. J., Crawford, J. H.: Application of OMI observations to a space-based indicator of NO<sub>x</sub> and VOC controls on surface ozone formation, *J. Atmos. Env.*, 44, 2213-2223, doi:10.1016/j.atmosenv.2010.03.010, 2010.
- Drummond, J.W., Volz, A., and Ehhalt, D. H.: An optimized chemiluminescence detector for tropospheric NO measurements, *J. Atmos. Chem.*, 2, 287–306, doi:10.1007/BF00051078, 1985.
- Fischer, H., Pozzer, A., Schmitt, T., Jöckel, P., Klippel, T., Taraborrelli, D., and Lelieveld, J.: Hydrogen peroxide in the marine boundary layer over the South Atlantic during the OOMPH cruise in March 2007, *Atmos. Chem. Phys.*, 15, 6971-6980, doi:10.5194/acp-15-6971-2015, 2015.
- Hauglustaine, D. A., Madronich, S., Ridley, B. A., Walega, J. G., Cantrell, C. A., and Shetter, R. E.: Observed and model-calculated photostationary state at Mauna Loa Observatory during MLOPEX 2, *J. Geophys. Res.*, 101, 14681-14696, doi:10.1029/95JD03612, 1996.
- Hens, K., Novelli, A., Martinez, M., Auld, J., Axinte, R., Bohn, B., Fischer, H., Keronen, P., Kubistin, D., Nölscher, A. C., Oswald, R., Paasonen, P., Petäjä, T., Regelin, E., Sander, R., Sinha, V., Sipilä, M., Taraborrelli, D., Tatum Ernest, C., Williams, J., Lelieveld, J., Harder, H.: Observation and modelling of HO<sub>x</sub> radicals in a boreal forest, *Atmos. Chem. Phys.*, 14, 8723-8747, doi:10.5194/acp-14-8723-2014, 2014.
- Hernandez, M. D. A., Burkert, J., Reichert, L., Stöbener, D., Meyer-Arne, J., and Burrows, J. P.: Marine boundary layer peroxy radical chemistry during the AEROSOLS99 campaign: Measurements and analysis, *J. Geophys. Res.*, 106, 20833-20846, doi:10.1029/2001JD900113, 2001.
- Hollaway, M. J., Arnold, S. R., Challinor, A. J., and Emberson, L. D.: Intercontinental trans-boundary contributions to ozone-induced crop yield losses in the Northern Hemisphere, *Biogeosciences*, 9, 271-292, doi:10.5194/bg-9-271-2012, 2012.
- Hosaynali Beygi, Z., Fischer, H., Harder, H. D., Martinez, M., Sander, R., Williams, J., Brookes, D. M., Monks, P. S., and Lelieveld, J.: Oxidation photochemistry in the Southern Atlantic boundary layer: unexpected deviations of photochemical steady state, *Atmos. Chem. Phys.*, 11, 8497-8513, doi:10.5194/acp-11-8497-2011, 2011.
- Jaffe, D. A., Cooper, O. R., Fiore, A. M., Henderson, B. H., Tonnesen, G. S., Russell, A. G., Henze, D. K., Langford, A. O., Lin, M., and Moore, T.: Scientific assessment of background ozone over the U.S.: Implications for air quality management, *Elem. Sci. Anth.*, 6, 56, doi:10.1525/elementa.309, 2018.

- 750 Javed, U., Kubistin, D., Martinez, M., Pollmann, J., Rudolf, M., Parchatka, U., Reiffs, A., Thieser, J., Schuster, G., Horbanski, M., Pöhler, D., Crowley, J. N., Fischer, H., Lelieveld, J., and Harder, H.: Laser-induced fluorescence-based detection of atmospheric nitrogen dioxide and comparison of different techniques during the PARADE 2011 field campaign, *Atmos. Meas. Tech.*, 12, 1461-1481, doi:10.5194/amt-12-1461-2019, 2019.
- Jöckel, P., Kerkweg A., Pozzer, A., Sander, R., Tost, H., Riede, H., Baumgartner, A., Gromov, S., and Kern, B.: Development of cycle 2 of the Modular Earth Submodel System (MESSy2), *Geosci. Model Dev.*, 3, 717-752, doi:10.5194/gmd-3-717-2010, 2010.
- 755 Johansson, L., Jalkanen, J.-P., Kukkonen, J.: Global assessment of shipping emissions in 2015 on a high spatial a temporal resolution, *J. Atmos. Env.*, 167,403-415, doi:10.1016/j.atmosenv.2017.08.042., 2017.
- Keller-Rudek, H., Moortgat, G. K., Sander, R., and Sörensen, R.: The MPI-Mainz UV/VIS Spectral Atlas of Gaseous Molecules of Atmospheric Interest, *Earth Syst. Sci. Data*, 5, 365-373, doi:10.5194/essd-5-365-2013, 2013.
- 760 Kleinman, L. I., Daum, P. H., Lee, Y.-N., Nunnermacker, L. J., Springston, S. R. Weinstein-Lloyd, J., and Rudolph, J.: A comparative study of ozone production in five U.S. metropolitan areas, *J. Geophys. Res.-Atmos.*, 110, D02301, doi:10.1029/2004jd005096, 2005.
- Klonecki, A. and Levy, H.: Tropospheric chemical ozone tendencies in CO-CH<sub>4</sub>-NO<sub>y</sub>-H<sub>2</sub>O system: Their sensitivity to variations in environmental parameters and their application to a global chemistry transport model study, *J. Geophys. Res.*, 102, 21221–21237, doi:10.1029/97JD01805, 1997.
- 765 Kormann, R., Fischer, H., de Reus, M., Lawrence, M., Brühl, Ch., von Kuhlmann, R., Holzinger, R., Williams, J., Lelieveld, J., Warneke, C., de Gouw, J., Heland, J., Ziereis, H., and Schlager, H.: Formaldehyde over the eastern Mediterranean during MINOS: Comparison of airborne in-situ measurements with 3D-model results, *Atmos. Chem. Phys.*, 3, 851-861, doi:10.5194/acp-3-851-2003, 2003.
- 770 Kouvarakis, G., Vrekoussis, M., Mihailopoulos, N., Kourtidis, K., Rappenglueck, B., Gerasopoulos, E., and Zerefos, C.: Spatial and temporal variability of tropospheric ozone (O<sub>3</sub>) in the boundary layer above the Aegean Sea (eastern Mediterranean), *J. Geophys. Res.*, 107, D18, 8137, doi:10.1029/2000JD000081, 2002.
- Krotkov, N. A., McLinden, C. A., Li, C., Lamsal, L. N., Celarier, E. A., Marchenko, S. V., Swartz, W. H., Bucsela, E. J., Joiner, J., Duncan, B. N., Boersma, K. F., Veefkind, J. P., Levelt, P. F., Fioletov, V. E., Dickerson, R. R., He, H., Lu, Z., and

- Streets, D. G.: Aura OMI observations of regional SO<sub>2</sub> and NO<sub>2</sub> pollution changes from 2005 to 2015, *Atmos. Chem. Phys.*, 16, 4605–4629, doi:10.5194/acp-16-4605-2016, 2016.
- Kwok, C. Y., Laurent, O., Guemri, A., Philippon, C., Wastine, B., Rella, C. W., Vuillemin, C., Truong, F., Delmotte, M., Kazan, V., Darding, M., Lebegue, B., Kaiser, C., Xueref-Remy, I., and Ramonet, M.: Comprehensive laboratory and field testing of cavity ring-down spectroscopy analyzers measuring H<sub>2</sub>O, CO<sub>2</sub>, CH<sub>4</sub> and CO, *Atmos. Chem. Phys.*, 8, 3867–3892, doi:10.5194/amt-8-3867-2015, 2015.
- Leighton, P. A.: Photochemistry of air pollution, *Phys. Chem.*, 9, 1961.
- Lelieveld, J., Dentener, F. J., Peters, W., and Krol, M. C.: On the role of hydroxyl radicals in the self-cleansing capacity of the troposphere, *Atmos. Chem. Phys.*, 4, 2337–2344, doi:10.5194/acp-4-2337-2004, 2004.
- 785 Lelieveld, J., Hoor, P., Jöckel, P., Pozzer, A., Hadjinicolaou, P., Cammas, J.-P., and Beirle, S.: Severe ozone air pollution in the Persian Gulf region, *Atmos. Chem. Phys.*, 9, 1393–1406, doi:10.5194/acp-9-1393-2009, 2009.
- Lelieveld, J.: Strongly increasing heat extremes in the Middle East and North Africa (MENA) in the 21<sup>st</sup> century, *Climate Change*, 137, 245–260, doi:10.1007/s10584-016-1665-6, 2016a.
- Lelieveld, J., Gromov, S., Pozzer, A., and Taraborrelli, D.: Global tropospheric hydroxyl distribution, budget and reactivity, *Atmos. Chem. Phys.*, 16, 12477–12493, doi:10.5194/acp-16-12477-2016, 2016b.
- 790 Liu, F., Beirle, S., Zhang, Q., Dörner, S., He, K., and Wagner, T.: NO<sub>x</sub> lifetimes and emissions of cities and power plants in polluted background estimated by satellite observations, *Atmos. Chem. Phys.*, 16, 5823–5298, doi:10.5194/acp-16-5283-2016, 2016.
- Lu, K., Zhang, Y., Su, H., Brauers, T., Chou, C., Hofzumahaus, A., Liu, S., Kita, K., Kondo, K., Shao, M., Wahner, A., Wang, J., Wang, X., and Zhu, T.: Oxidant (O<sub>3</sub>+NO<sub>2</sub>) production processes and formation in regimes in Beijing, *J. Geophys. Res.*, 115, D07303, doi:10.1029/2009JD012714, 2010.
- 795 Mallik, C., Tomsche, L., Bourtsoukidis, E., Crowley, J. N., Derstroff, B., Fischer, H., Hafermann, S., Hüser, I., Javed, U., Keßel, S., Lelieveld, J., Martinez, M., Meusel, H., Novelli, A., Phillips, G. J., Pozzer, A., Reiffs, A., Sander, R., Taraborrelli, D., Sauvage, C., Schuladen, J., Su, H., Williams, J., and Harder, H.: Oxidation processes in the eastern Mediterranean atmosphere: evidence from the modelling of HO<sub>x</sub> measurements over Cyprus, *Atmos. Chem. Phys.*, 18, 10825–10847, doi:10.5194/acp-18-10825-2018, 2018.
- 800

- Mannschreck, K., Gilge, S., Plass-Duelmer, C., Fricke, W., and Berresheim, H.: Assessment of the applicability of NO-NO<sub>2</sub>-O<sub>3</sub> photostationary state to long-term measurements at the Hohenpeissenberg GAW Station, Germany, *Atmos. Chem. Phys.*, 4, 1265-1277, doi:10.5194/acp-4-1265-2004, 2004.
- 805 Mao, J., Ren, X., Chen, S., Brune, W. H., Chen, Z., Martinez, M., Harder, H., Lefer, B., Rappenglück, B., Flynn, J., Leuchner, M.: Atmospheric oxidation capacity in the summer of Houston 2006: Comparison with summer measurements in the metropolitan studies, *Atmos. Environ.*, 44, 4107-4115, doi:10.1016/j.atmosenv.2009.01.013, 2009.
- Martin R., Fiore, A., Van Donkelaar, A. 2004: Space-based diagnosis of surface ozone sensitivity to anthropogenic emissions, *Geophys. Res. Lett.*, 31, L06120, doi:10.1029/2004GL019416, 2004.
- 810 Martinez, M., Harder, H., Kubistin, D., Rudolf, M., Bozem, H., Eerdekens, G., Fischer, H., Klüpfel, T., Gurk, C., Königstedt, R., Parchatka, U., Schiller, C. L., Stickler, A., Williams, J., and Lelieveld, J.: Hydroxyl radicals in the tropical troposphere over the Suriname rainforest: airborne measurements, *Atmos. Chem. Phys.*, 10, 3759-3773, doi: 10.5194/acp-10-3759-2010, 2010.
- Mazzuca G. M., Ren, X., Loughner, C. P., Estes, M., Crawford, J. H., Pickering, K. E., Weinheimer, A. J., and Dickerson, R.
- 815 R.: Ozone production and its sensitivity to NO<sub>x</sub> and VOCs: results from the DISCOVER-AQ field experiment, Houston 2013, *Atmos. Chem. Phys.*, 16, 14463-14474, doi:10.5194/acp-16-14463-2016, 2016.
- Meusel, H., Kuhn, U., Reiffs, A., Mallik, C., Harder, H., Martinez, M., Schuladen, J., Bohn, B., Parchatka, U., Crowley, J. N., Fischer, H., Tomsche, L., Novelli, A., Hoffmann, T., Janssen, R. H. H., Hartogensis, O., Pikridas, M., Vrekoussis, M., Bourtsoukidis, E., Weber, B., Lelieveld, J., Williams, J., Pöschl, U., Cheng, Y., and Su, H.: Daytime formation of nitrous acid
- 820 at a coastal remote site in Cyprus indicating a common ground source of atmospheric HONO and NO, *Atmos. Chem. Phys.*, 16, 14475-14493, doi:10.5194/acp-16-14475-2016, 2016.
- Miyazaki, K., Eskes, H., Sudo, K., Folkert Boersma, K., Bowman, K., and Kanaya, Y.: Decadal changes in global surface NO<sub>x</sub> emissions from multi-constituent satellite data assimilation, *Atmos. Chem. Phys.*, 17, 807-837, doi:10.5194/acp-17-807-2017, 2017.
- 825 Monks, P. S., Archibald, A. T., Colette, A., Cooper, O. Coyle, M., Derwent, R., Fowler, D., Granier, C., Law, K. S., Mills, G. E., Stevenson, D. S., Tarasova, O., Thouret, V., von Schneidemesser, E., Sommariva, R., Wild, O., Williams, M. L.: Tropospheric ozone and its precursors from the urban to the global scale from air quality to short-lived climate forcer, *Atmos. Chem. Phys.*, 15, 8889-8973, doi:10.5194/acp-15-8889-2015, 2015.

- Nakamura, K., Kondo, Y., Chen, G., Crawford, J. H., Takegawa, N., Koike, M., Kita, K., Miyazaki, Y., Shetter, R. E., Lefer, B. L., Avery, M., and Matsumoto J.: Measurement of NO<sub>2</sub> by the photolysis conversion technique during the Transport and Chemical Evolution Over the Pacific (TRACE-P) campaign, *J. Geophys. Res.*, 108, D24, 4752, doi:10.1029/2003JD003712, 2003.
- Parrish, D. D., Trainer, M., Williams, E. J., Fahey D. W., Hübler, G., Eubank, C. S., Liu S. C., Murphy, P. C., Albritton, D. L., Fehsenfeld, F. C.: Measurements of the NO<sub>x</sub>-O<sub>3</sub>-photostationary steady state at Niwot Ridge, Colorado, *J. Geophys. Res.*, 91, 5361-5370, doi:10.1029/JD091iD05p05361, 1986.
- Pollack, I. B., Lerner, B. M., Ryerson, T. B.: Evaluation of ultraviolet light-emitting diodes for detection of atmospheric NO<sub>2</sub> by photolysis – chemiluminescence, *J. Atmos. Chem.*, 65, 111-125, doi:10.1007/s10874-011-9184-3, 2011.
- Pfannerstill, E. Y., Wang, N., Edtbauer, A., Bourtsoukidis, E., Crowley, J. N., Dienhart, D., Eger, P. G., Ernle, L., Fischer, H., Hottmann, B., Paris, J.-D., Stönnner, C., Tadic, I., Walter, D., Lelieveld, J., Williams, J.: Shipborne measurements of total OH reactivity around the Arabian Peninsula and its role in ozone chemistry, *Atmos. Chem. Phys.*, 19, 11501-11523, doi:10.5194/acp-19-11501-2019, 2019.
- Reed, C., Evans, M. J., Di Carlo, P., Lee, J. D., and Carpenter, L. J.: Interferences in photolytic NO<sub>2</sub> measurements: explanation for an apparent missing oxidant?, *Atmos. Chem. Phys.*, 16, 4707-4724, doi:10.5194/acp-16-4707-2016, 2016.
- Regelin, E., Harder, H., Martinez, M., Kubistin, D., Tatum Ernest, C., Bozem, H., Klippel, T., Hosaynali Beygi, Z., Fischer, H., Sander, R., Jöckel, P., Königstedt, R., and Lelieveld, J.: HO<sub>x</sub> measurements in the summertime upper troposphere over Europe: a comparison of observations to a box model and a 3-D model, *Atmos. Chem. Phys. Phys.*, 13, 10703-10720, doi:10.5194/acp-13-10703-2013, 2013.
- Ren, X., van Duin, D., Cazorla, M., Chen, S., Mao, J., Zhang, L., Brune, W. H., Flynn, J. H., Grossberg, N., Lefer, B. L., Rappenglück, B., Wong, K. W., Tsai, C., Stutz, J., Dibb, J. E., Jobson, B. T., Luke, W. T., and Kelley, P.: Atmospheric oxidation chemistry and ozone production: Results from SHARP 2009 in Houston, Texas, *J. Geophys. Res.*, 118, 5570-5780, doi:10.1002/jgrd.50342, 2013.
- Roeckner, E., Brokopf, R., Esch, M., Giorgetta, M., Hagemann, S., Kornblüeh, L., Manzini, E., Schlese, U., and Schulzweida, U.: Sensitivity of Simulated Climate to Horizontal and Vertical Resolution in the ECHAM5 Atmosphere Model, *J. Climate*, 19, 3771-3791, doi:10.1175/JCLI3824.1, 2006.

- 855 Ryerson, T. B., Williams, E. J., and Fehsenfeld, F. C.: An efficient photolysis system for fast-response NO<sub>2</sub> measurements, *J. Geophys. Res.*, 105, D21, 26447-26461, doi:10.1029/2000JD900389, 2000.
- Sander, R., Baumgartner, A., Cabrera-Perez, D., Frank, F., Gromov, S., Grooß, J.-U., Harder, H., Huijnen, V., Jöckel, P., Karydis, V. A., Niemeyer, K. E., Pozzer, A., Riede, H., Schultz, M. G., Taraborrelli, D., and Tauer, S.: The community atmospheric chemistry box model CAABA/MECCA-4.0, *Geosci. Model Dev.*, 12, 1365-1385, doi: 10.5194/gmd-12-1365-2019, 2019.
- 860 Sobanski, N., Schuladen, J., Schuster, G., Lelieveld, J., and Crowley, J. N.: A five-channel cavity ring-down spectrometer for the detection of NO<sub>2</sub>, NO<sub>3</sub>, N<sub>2</sub>O<sub>5</sub>, total peroxy nitrates and total alkyl nitrates, *Atmos. Meas. Techn.*, 9, 5103-5118, doi:10.5194/amt-9-5103-2016, 2016.
- Sillman, S., Al-Wali, K., Marsik, F. J., Nowacki, P., Samson, P. J., Rodgers, M. O., Garland, L. J., Martinez, J. E., Stoneking, C., Imhoff, R., Lee, J. H., Newman, L., Weinstein-Lloyd, J., and Aneja, V.: Photochemistry of ozone formation in Atlanta, GA - models and measurements, *Atmos. Environ.*, 29, 21, 3055-3066., doi:10.1016/1352-2310(95)00217-M, 1995.
- 865 Thornton, J. A., Wooldridge, P. J., Cohen, R. C., Martinez, M., Harder, H., Brune, W. H., Williams, E. J., Roberts, J. M., Fehsenfeld, F. C., Hall, S. R., Shetter, R. E., Wert, B. P., and Fried, A.: Ozone production rates as a function of NO<sub>x</sub> abundances and HO<sub>x</sub> production rates in the Nashville urban plume, *J. Geophys. Res.*, 107, D12, doi:10.1029/2001JD000932, 2002.
- 870 Tuzson, B., Zeyer, K., Steinbacher, M., McManus, J. B., Nelson, D. D., Zahniser, M. S., and Emmenegger, L.: Selective measurements of NO, NO<sub>2</sub> and NO<sub>y</sub> in the free troposphere using quantum cascade laser spectroscopy, *Atmos. Meas. Tech.*, 6, 927-936, doi:10.5194/amt-6-927-2013, 2013.
- Viallon, J., Lee, S., Moussay, P., Tworek, K., Petersen, M., and Wielgosz, R. I.: Accurate measurements of ozone absorption cross-sections in the Hartley band, *Atmos. Meas. Tech.*, 8, 1245-1257, doi:10.5194/amt-8-1245-2015, 2015.
- 875 Velchev, K., Cavalli, F., Hjorth, J., Vignati, E., Dentener, F., and Raes, F.: Ozone over the Western Mediterranean Sea – results from two years of shipborne measurements, *Atmos. Chem. Phys.*, 11, 675-688, doi:10.5194/acp-11-675-2011, 2011.
- Zhou, W., Cohan, D. S., and Henderson, B. H.: Slower ozone production in Houston, Texas following emission reductions: evidence from Texas Air Quality Studies in 2000 and 2006, *Atmos. Chem. Phys.*, 14, 2777-2788, doi:10.5194/acp-14-2777-2014, 2014.